Development of a Scintillator Cluster Detector and Microcontroller Integrated Detector Circuit

David Barraclough

Master of Science by Research

University of York
Physics, Engineering and Technology

December 2023

Abstract

This thesis reports on the development of a prototype cluster scintillator detector hermetically sealed in an aluminium housing for use in the HYPATIA array. The HYPATIA array will consist of GaGG and CeBr3(Ce) scintillators, however, this prototype uses four NaI(Tl) crystals to optimise the design and validate the encapsulation process before the final device is constructed. The NaI(Tl) crystals, 30x30x80mm were mounted to 2x2 SiPM arrays. The energy and time resolution, energy calibration and linearity of the detector were measured for each detector element as well as add-back being used for each detector pairing. The long-term performance of the hermetic seal was tested over a two-month period and showed no degradation in detector performance outside of measurement error. The best performing crystal had a FWHM energy resolution of 7.79±0.02% while the FWHM coincidence time resolution between a pair of crystals was 23.1±0.2ns. A proposal for a redesign of the aluminium housing and associated clamping system is also presented. The redesign aims to minimise the external dimensions of the can and in particular its lid in order to enable the detector to better fit with other detectors of the same design in the HYPATIA array. The suggested redesign allows for a closer packing of the quad clusters in the array, reducing the dead space within the active solid angle of the array from 8.5±0.1% to 2.2±0.4%.

Also reported on in this thesis is the development of a microcontroller integrated detector circuit. This circuit used an Arduino Nano BLE33 microcontroller on a solderless breadboard with a peak hold circuit. The circuit had a maximum nonlinearity of 1.24±0.03% and an average FWHM channel resolution of 44.5±0.2. The motivation behind this work was to extend the use of the Hypatia cluster into the societal applications regime by enabling a portable, high efficiency scintillator detector.

The conclusions from the present study regarding the performance of the prototype cluster detector validate the technological choices for the assembly methods and materials for canning and informs future choices for the final HYPATIA clusters.

Table of Contents

Declaration

I declare that this thesis is a presentation of original work, and I am the sole author. This work has not previously been presented for a degree or other qualification at this University or elsewhere. All sources are acknowledged as references.

Acknowledgments

I would like to acknowledge and express my gratitude to a number of people who have made contributions to this project. Firstly, I would like to thank my supervisor Stefanos Paschalis, his continued guidance and weekly meetings have been invaluable throughout the project. I would like to thank the many members of the York Nuclear Physics group who have offered their assistance and advice whenever I needed it.

Additionally, I would like to thank Timothy Ayers of York Physics, Engineering and Technology Electronics Workshop without whom the electronics portion of this project would not have been possible.

Table of Figures

1 Introduction

All visible matter in the known universe is comprised of atoms. They constitute all the material that we interact with on a daily basis. At the centre of the atom is the nucleus, the radius of which is around 100,000 times less than that of the atom it is in. However, the nucleus constitutes around 99% of all visible matter in the known universe. It is for this reason that understanding the nucleus is so important to modern physics. However, making observations of and probing an environment on such a microscopic scale was for much of our history impossible. Despite this many experiments have managed to gain insight into the structure and composition of the atom.

One of the modern experimental methods used to study the atom and nuclear structure is in-beam γ ray spectroscopy. This involves using a fast particle beam that is directed at a reaction target. A large γ ray detector array surrounding the target then measures the resultant radiation. This method can produce a number of useful observables such as excited state energies, differential cross sections, deformation lengths and state lifetimes. This project looks to develop a hermetically sealed scintillator detector prototype for an in-beam γ ray spectroscopy array, the HYPATIA array (HYbrid Photon detector Array To Investigate Atomic nuclei) at the Radio Isotope Beam Factory (RIBF) in Japan.

1.1 A History of Scintillation Detectors

The discovery of the atomic nucleus was made by Ernest Rutherford in 1911. By conducting the famous α particle scattering experiment [1], he discovered the true nature of the central nucleus containing 99.9% of the atom's mass. The experiment relied on the detection of α particles after they scattered on a sheet of gold foil. This was done using screens coated with Zinc Sulphide, when an α particle struck the screen the ZnS would fluoresce. These scintillation events were observed using a microscope and then manually counted. This was one of the first examples of a scintillation-based detection method.

Scintillator detectors have a long history in the detection of ionising radiation and have been used in many experiments that have probed the core of the atom. To that end, the following section presents a brief history of scintillator detection and the key technologies that have enabled it.

1.1.1 Photomultiplier tubes

The earliest methods of scintillation detection that employed fluorescent screens relied upon the manual counting of individual light pulses. This was a tedious process which limited the practicality of scintillator detectors. This was changed however, with the invention of the photomultiplier tube (PMT). The first PMT was produced in 1930 by L. A. Kubetsky [2]. This device operated via multistage secondary emission. The output of stage one was sent to the secondary stage which used secondary emission to amplify the output. Then in 1936 this design was improved further by Vladimir Zworykin et al. [3] to have a high gain operation. This version had a maximum gain of 60, within a year this gain had been increased to around 1000 by Kubetsky [4]. At the same time as these developments were taking place a new photoelectric material was discovered, Cs3Sb [5]. This material had a much greater quantum efficiency, further improving the efficiency of PTMs. PMTs are still a widely used technology today. The predecessor to the HYPATIA array, the DALI2+ array, used PMTs for all its scintillator detectors.

1.1.2 The Development of Solid-State Photodetectors

Around the time of the development of the PMT, one of the first observations of photo-effects of Silicon and Germanium was made by F.C. Nix in 1932 [6]. Later in 1940 R. Ohl made the same observation when studying an ingot of silicon [7] and patented his photosensitive device. These discoveries were some of the first in a growing area of research dedicated to the photosensitivity of semiconductors.

In 1951 a device that was able to be used as an optical detector was developed by W. Pietenpol [8]. This device was an example of a phototransistor, which were the first solid-state optical sensors. The first example of a photodiode that used avalanche breakdown to increase the gain (an APD) was developed by J. Nishizawa in 1952 [9]. This device and other similar devices developed around this time, like the work done at Shockley labs [10], still did not have the ability to detect single photons. However, they did pave the way for modern devices such as the Single Photon Avalanche Diode (SPAD) and the SiPM.

The development of these devices over many years has led to the current technology that is now the primary photodetection method for scintillator detectors. Solid-state devices offer a good quantum efficiency, often superior to that of PMTs, and very high resolutions. An additional advantage of device like SiPMs over PMTs is that they are not prohibited by magnetic fields.

1.1.3 Developments in Inorganic Scintillating materials

As discussed in section 1.1.1 the early use of scintillators, before the invention of the PMT or the photodiode, involved visually counting scintillation events. Examples of this are $CaWO_4$ and uranyl which were used by Becquerel to discover radioactivity. However, the discovery of NaI(Tl) By R. Hofstadter [11] in 1948 sparked investigation into scintillating materials. Many of the scintillators developed in this period (1940-1960) are still used widely today like NaI(Tl) and CsI(Tl). These developments focused heavily on alkali halide crystals and naturally occurring phosphors.

The development of non-naturally occurring materials for scintillators began predominantly after the 1980s. During this time materials such as $Bi_4Ge_3O_{12}$ (BGO) [12] were developed. The synthesis of scintillation compounds enabled the development of scintillators with much higher effective atomic masses than naturally occurring ones, BGO being one of these high effective atomic mass materials. A notable development from this era was the research done into Ce doping of insulating materials. Ce doping has become a standard method in scintillator development. This is due to its allowed optical 5d-4f transition, which is typically around 20-40ns, and can be doped onto many high-density host materials [13]. An example of this is the development of Ce-doped Lutetium Oxyorthosilicate (LSO(Ce)) [14] which has a decay time of around 40ns. The development of common scintillators is depicted below in Figure 1.1.

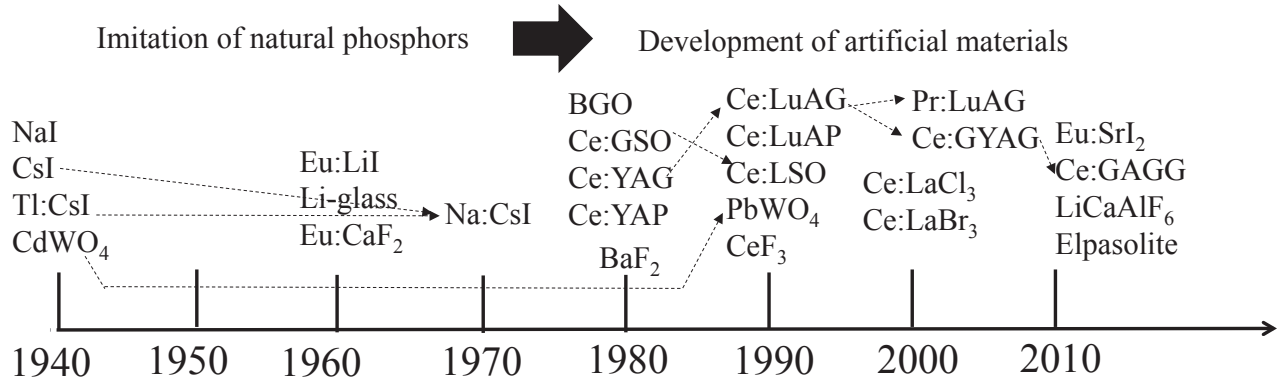

Figure 1.1: Diagram depicting the development of common scintillator materials. The two eras of development of natural and artificial materials are shown at the top of the Figure. The dotted arrows show modifications made to known materials to produce a new material. [15]

Modern day inorganic scintillator research has become focused on developing highly specialised scintillating materials for specific applications. For example, security applications require very high energy resolutions, around 2-3%, however, timing resolution is not as important as it is for many fundamental physics applications. A result

of this is that many modern detector designs employ a hybrid approach, using multiple different scintillating materials. This enables a detector or array to use the best properties of each material. The HYPATIA array is an example of such an array. The array looks to use CeBr3 scintillator detectors in the barrel for their fast-timing resolution and GAGG(Ce) at forward angles due to their high resolution and high effective atomic mass.

The GAGG(Ce) (Gadolinium Aluminium Gallium Garnet) scintillator represents a recent development in oxide scintillators. GAGG(Ce) can have a light output of up to 70,000 ph/MeV [16]. This significantly closes the gap between oxide scintillators and halide scintillators which have traditionally had superior light output.

1.2 Development of a Hermetically Sealed Scintillator Detector

The HYPATIA array, which this project looked to develop a prototype detector for, is shown in Figure 1.2. This array is an upgrade to the pre-existing Detector Array for Low Intensity radiation 2+ (DALI2+) at RIBF. The original DALI array began operation in 1992 and was designed to observe nuclear reactions with a low yield [17]. It contained 60 NaI(Tl) detectors that covered a large solid angle. This array was replaced by DALI2 in 2002 when it was upgraded to accommodate up to 186 NaI(Tl) detectors which had a typical resolution of 9% at 661.7KeV (the ^{137}Cs standard) [18]. These detectors covered a range of polar angles in the laboratory frame between 15° and 160°. A list of experiments conducted at with DALI and DALI2 can be found in [18]. In 2017 the array was further upgraded to DALI2+. This upgrade added 40 new detectors bringing the total to 226 [18].

The HYPATIA array is an upgrade from the DALI2+ array. The final array will have all NaI(Tl) detectors at larger angles to the beam direction replaced by CeBr3 detectors, this will make up the barrel section of the detector. In the forward beam direction after the reaction target, the NaI(Tl) detectors will be replaced by GAGG(Ce) detectors. This is shown in Figure 1.2. The CeBr3 detectors have been selected due to their improved resolution over NaI(Tl), typically around 4% at 661.7 keV [19], and their fast decay time. GAGG detectors have a high effective atomic mass making it a good candidate for detecting higher energy γ rays that are emitted in the forward direction due to Lorenz boost in the forward direction.

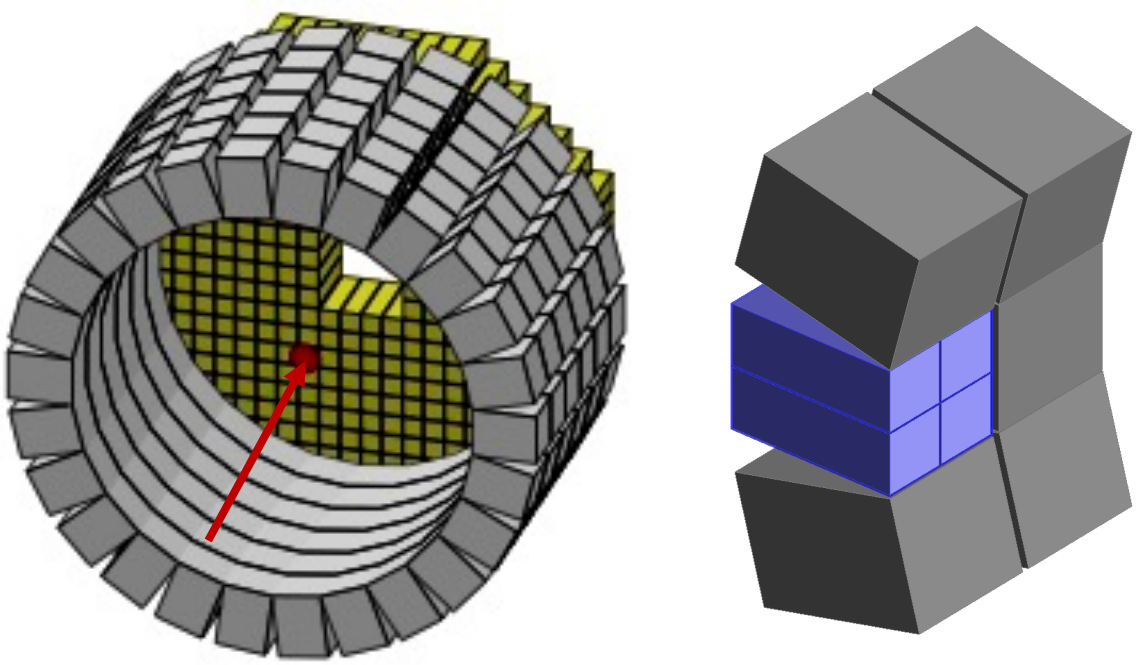

Figure 1.2: Model of full HYPATIA array (left), the grey cubes show the CeBr3 detectors with the GAGG(Ce) detectors shown in yellow. Close-up view of six CeBr3 within the HYPATIA array (right). One detector shows the four scintillator crystals inside it (blue) and the direction of the radio isotope beam is shown by a red arrow. [20] [21]

The CeBr3 scintillator crystals suffer from hygroscopicity, meaning that they degrade when exposed to moisture and need to be hermitically sealed. The development of the prototype for such a housing was the primary aim of this project. This housing had to accommodate four 30x30x80 mm crystals as well as stack together with other identical detectors in an array as Figure 1.2 shows. A low atomic number material had to be used to reduce any absorption of photons by the housing, so aluminium was selected. Another requirement was for the crystals to be optically isolated. This was to allow for add-back to be done to enable doppler shift correction. An initial design produced by the York Physics, Engineering and Technology (PET) machine workshop was tested in both detector performance and hermetic seal performance. A revision of this design with the aim of improving the fitment in the array was then proposed and is presented in this report.

1.3 Development of a Microcontroller Integrated Circuit

Alongside the development of a hermetically sealing detector housing, this project also aimed to develop a microcontroller integrated detector circuit which could be used for a range of applications such as data acquisition, temperature monitoring and have additional functions like GPS data. While this development was not intended to compete with the high-end nuclear instrumentation readout systems used for the gamma-ray spectrometers, it aimed to develop a low-cost, lightweight, and versatile, multi-channel readout system that could extend the applications of the HYPATIA cluster in the direction of nuclear security and environmental monitoring where portability is essential. York Nuclear Physics Group has a history of collaborating with companies to assist in the production and development of portable nuclear detector devices. However, the aim of this section of the project was to develop a fully inhouse built circuit using a publicly available microcontroller. One of the main motivating factors for this was the modularity that using a microcontroller and building the device inhouse enables. Constructing a detector circuit in this way gives great customisability over purchasing a prebuilt detector module.

The portability of such a device was also an important factor and was another motivating factor to use a microcontroller. This was important to keep the range of applications suitable for this device as wide as possible for example, nuclear security and environmental monitoring. The microcontroller selected, the Arduino Nano BLE33, has Bluetooth built in. Although the Bluetooth capabilities were not investigated in this project, this enabled future work to build on the platform developed in this project.

The resolution and linearity performance of the device was tested, and a new design was put forward and presented in this report. The device was intended to be used in conjunction with the hermetically sealed detector developed in the first part of the project, however, due to time constraints of the project and technical difficulties, this was not possible.

2 Background

2.1 Gamma decay

Gamma decay is a mechanism of radioactive decay that naturally unstable nuclei or excited nuclei undergo. It allows a nucleus to fall from an unstable excited state to a lower more stable state. The nucleus spontaneously transitions from an initial excited state and falls to a lower energy state. The energy difference between the two states is given off in the form of a γ ray photon. Eq. 2.1 shows this with E_γ being the energy of the emitted γ ray, E_i the energy of the initial state and E_f the energy of the final state.

$$E_\gamma = \Delta E = E_i - E_f \tag{2.1}$$

This process often occurs after a beta decay or the emission of an alpha particle as the nucleus can often be unstable after such an event. An example of this is the decay of ^{137}Cs which most commonly emits a 661.7keV γ ray. The ^{137}Cs atom undergoes beta decay to ^{137}Ba this results in the nucleus being in an excited state of 661.7 keV. The 661.7 keV γ rays arise from these excited ^{137}Ba nuclei decaying down to their ground state. γ rays emitted like this tend to have an energy between 0.1MeV and 10MeV due to the differences between energy levels of nuclei. These excited states have a lifetime associated with them (the time taken for them to decay down to a lower state). The CeBr3 scintillator detectors that are to be used in the HYPATIA array have been selected in large part for their timing resolution, to attempt to directly measure lifetimes of exited states. These measurements can yield information about the structure of the nucleus that emitted the γ ray.

The decays of these excited nuclei do not necessarily transition directly from the excited state to the ground state. This can happen via a γ ray cascade where multiple γ rays are emitted in coincidence. In order to discern between these cascade events and lower

energy transition γ ray events that are detected in coincidence, they are grouped together as single emission events. Detecting these γ ray cascades can give much more information regarding the structure of the nucleus than just detecting single γ rays.

The detector developed in this project was intended as a prototype for a detector to be used for in-beam γ ray spectroscopy experiments. These experiments measure the γ ray emissions of ions that are inflight after a reaction target has been struck. This means, due to the high velocity of the ions, that the doppler shift of the γ ray energies becomes a large contributing factor in these experiments. This shift varies on both the velocity of the emitting ions, v, and the angle at which the γ ray interacts with the detector relative to the ion beam, θ_γ. Eq. 2.2 shows this relationship where E_{Lab} is the energy measured in the lab frame, E_0, is the transition energy and $\beta = v/c$.

$$E_{Lab} = E_0 \frac{\sqrt{1-\beta^2}}{1-cos\theta_\gamma} \tag{2.2}$$

2.2 Interaction of γ rays with matter

Understanding how γ rays interact with matter is crucial to understanding how we can detect them. Below is discussed the three main ways in which γ rays can interact with matter: the Photoelectric absorption, pair production, and Compton scattering.

2.2.1 Photoelectric Absorption

Photoelectric absorption is a process where a photon collides with an atom in the absorber material and is fully absorbed. The energy of the photon is absorbed by an electron in one of the absorber material atoms. If the energy of the photon is greater than that of the binding energy, E_b the electron is emitted from the atom as a photoelectron. In the case of γ rays with high enough energy, these photoelectrons are most likely to be emitted from the most tightly bound shell or the k shell. This is shown below in Figure 2.1 and the energy of the photoelectron, E_e, is given in Eq. 2.3 where E_b is the binding energy of the photoelectron in its initial shell.

$$E_e = h\nu - E_b \tag{2.3}$$

As well as the emitted photoelectron this process also creates an atom within the absorber material that is now ionised with a vacancy in a bound shell. The vacancy quickly gets filled through either rearrangement of electrons from other shells of the atom, recapture of a free electron in the material, or both. As a result, one or more characteristic X-ray photons or Auger electrons may be produced.

Photoelectric absorption is the dominant interaction process for γ rays in the 0.1MeV to 0.3MeV range. It is also more prevalent in materials with higher atomic numbers, Z. Eq. 2.4 shows an approximation for the probability of photoelectric absorption per atom, τ, where E_γ is the energy of the γ ray and n varies between 3-4 over the γ ray spectrum.

$$\tau \cong constant \times \frac{Z^n}{{E_\gamma}^{3.5}} \tag{2.4}$$

Similarly to photon attenuation varying with the atomic number of the material, the density of a material also affects photon attenuation. As the density of a material increases so does the attenuation of photons, this is described by the mass attenuation coefficient, μ , given in Eq. 2.5. I_0 is the initial intensity of photons, ρ is the density of the material and I is the intensity of the photons after traveling x cm in the material.

$$\mu = \rho \frac{\ln\left(\frac{I}{I_0}\right)}{\mathrm{x}} \tag{2.5}$$

Both Eq. 2.4 and 2.5 show that high atomic number and high-density materials such as lead offer absorption properties which makes them ideal for use in gamma ray shielding.

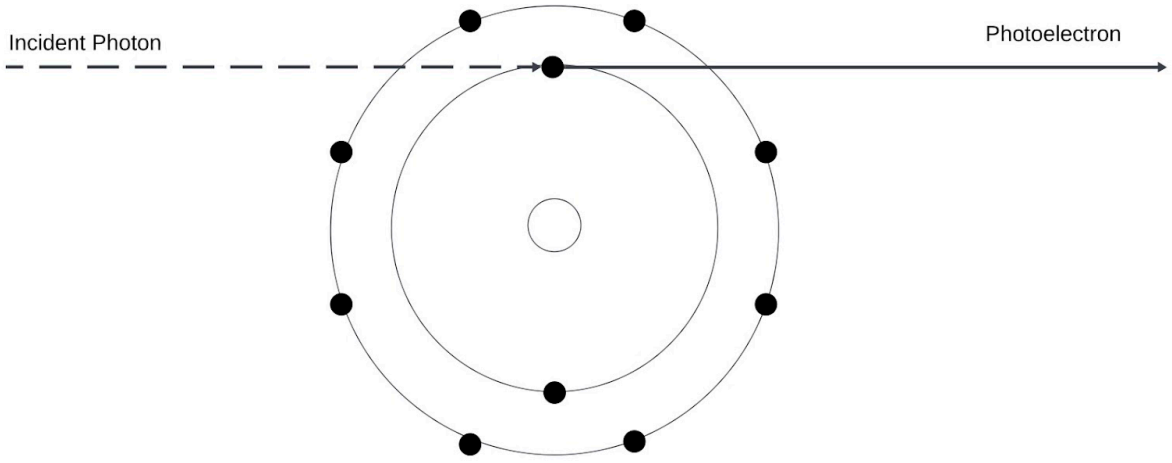

Figure 2.1: Diagram of Photoelectric absorption showing an incident electron being fully absorbed by a bound electron which is subsequently released as a photoelectron.

2.2.2 Pair Production

If a γ ray has energy above that of the rest mass energy of 2 electrons (1.022MeV [22]) then the electron may undergo the process of pair production. This interaction will take place in the Coulomb field of a nucleus in the absorber material. The probability of this occurring remains low until the γ ray reaches several MeV. The cross-section in the field of the nucleus, k_n, is approximately proportional to the square of the atomic number of the nucleus the interaction occurs in as shown in Eq.2.6 [23].

$$k_n \propto z^2 \tag{2.6}$$

The positron travels a short distance in the absorbing material before undergoing annihilation where the entire mass of the position is converted into energy in the form of two 511KeV photons. These photons are emitted at almost 180° to each other, dependant on the kinetic energy of the positron before annihilation. This process is shown below in figure 2.2.

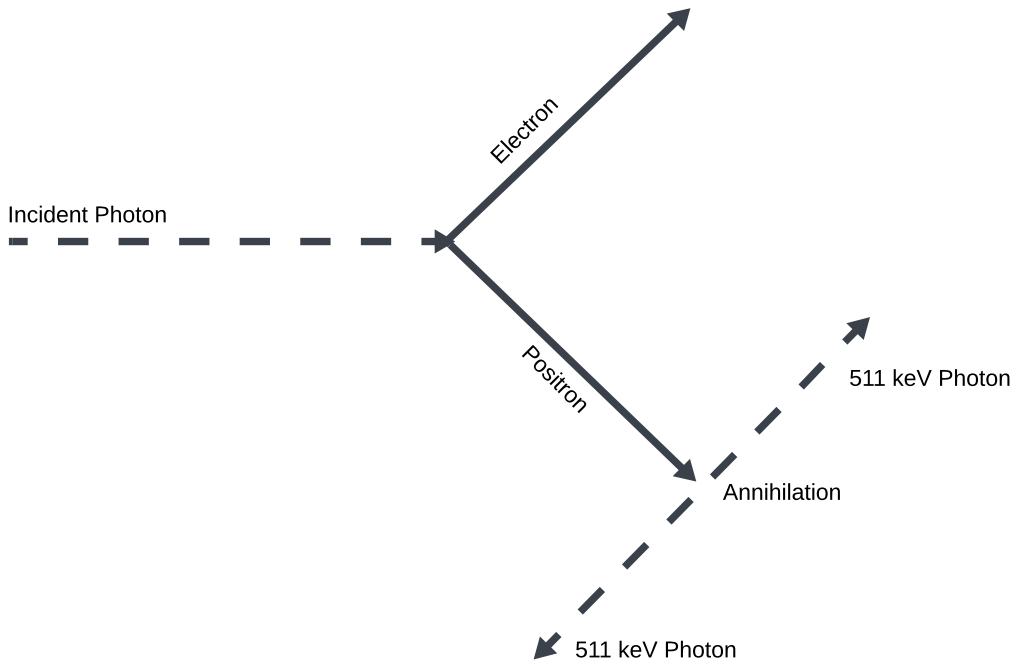

Figure 2.2: Diagram of pair production showing an incident photon >1.022MeV producing an electron and positron pair. The positron subsequently annihilates into two 511KeV photons which are emitted at almost 180°.

2.2.3 Compton Scattering

Compton scattering is a process that occurs between an incoming γ ray photon and an electron within the absorber material. An incoming photon is deflected through an angle θ, which is measured with respect to the original direction of the photon, due to a collision with an electron in the absorber material. This electron is imparted with some of the photon's energy, and it is itself deflected from its initial position where it was assumed to be at rest, it is now a recoil electron. The amount of energy transferred to the electron can range from most of the photon's energy to zero, depending on the angle of deflection. Eq. 2.7 relates the scattering angle of the photon (θ) to the energy transfer where m_0 is the rest mass of an electron, E_γ is the γ ray energy and c is the speed of light.

$$E_\gamma{}' = \frac{E_\gamma}{1 + \frac{E_\gamma}{m_0 c^2}(1 - \cos\theta)} \tag{2.7}$$

For small values of θ little energy is transferred and at any angle including the extreme case of the incident photon scattering backward (θ =π) some energy is retained by the incident photon.

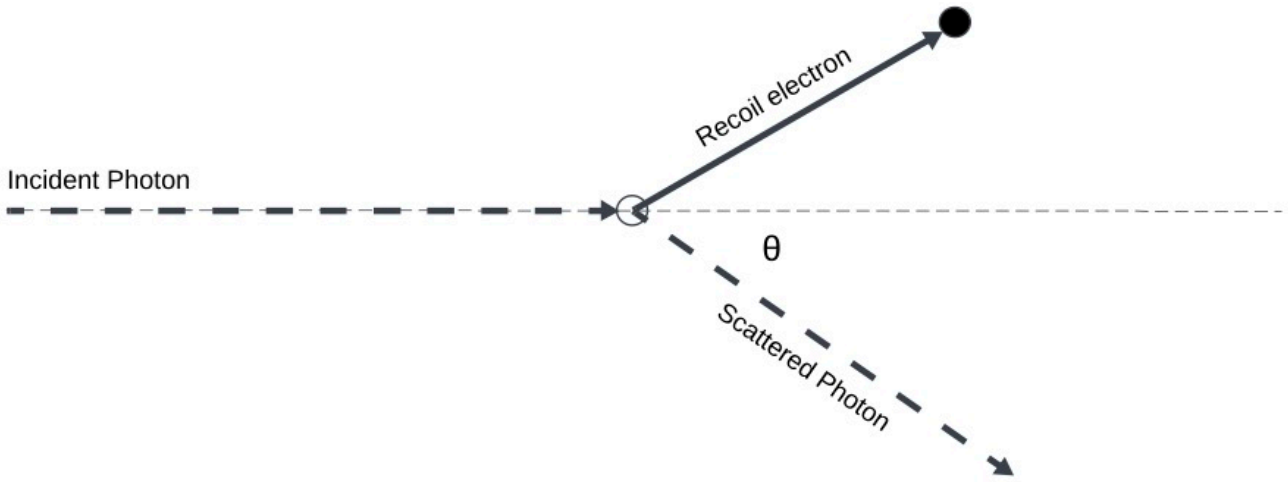

Figure 2.3: Diagram of Compton scattering showing an incident photon scattering off an electron at an angle **θ** measured relative to the initial trajectory of the photon**.**

The probability of Compton scattering occurring per atom depends on the number of electrons that photons can be scattered by. This means the cross scales linearly with Z. The angular distribution of scattered γ rays is given by the Klein-Nishina formula, Eq. 2.8.

This gives the differential scattering cross section $d\sigma/d\Omega$ where $\alpha \equiv h\nu/m_0c^2$ and r_0 is the classical electron radius. This equation is shown graphically below in Figure 2.4.

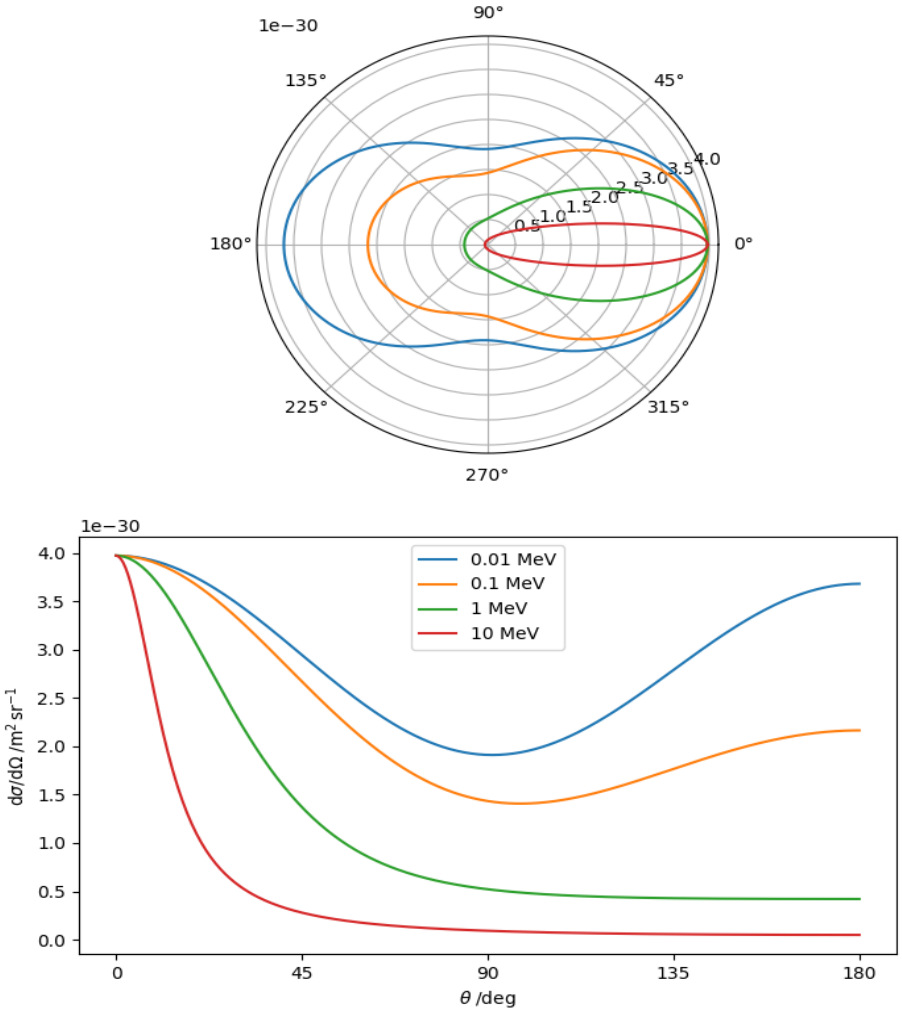

$$\frac{d\sigma}{d\Omega} = Z{r_0}^2 \left(\frac{1}{1+\alpha(1-cos\theta)}\right)^2 \frac{1+cos^2\theta}{2} 1 + \frac{\alpha^2(1-cos\theta)^2}{(1+cos^2\theta)} \tag{2.8}$$

Figure 2.4: Plot of Compton scattering angle probability for different photon energies. The top plot shows the plot in polar coordinates and the bottom plot show the same data

in cartesian coordinates. Both plots show the differential cross section per meter squared per square radian for a range of energies, shown in the legend, and show the tendency for higher energy photons to be scattered in the forward direction [24].

2.2.4 Total Photon Attenuation

All three of the mechanisms discussed above contribute to the attenuation of photons depending on the energy of the photon and the material the photon is in. Figure 2.5 shows the energy dependence for each interaction contributing to the total attenuation in NaI. It shows that at lower energies the photoelectric effect dominates and sharply increases at a few hundred keV. This is the K-absorption edge or the K-edge. It occurs at energies just above the binding energy of the K-shell electrons for the material, for γ rays above this energy the K-shell electrons can be emitted. However, below this binding energy, the electrons cannot be which causes a sudden drop in γ ray absorption. At higher energies pair production dominates, with a minimum energy requirement of 1.022MeV

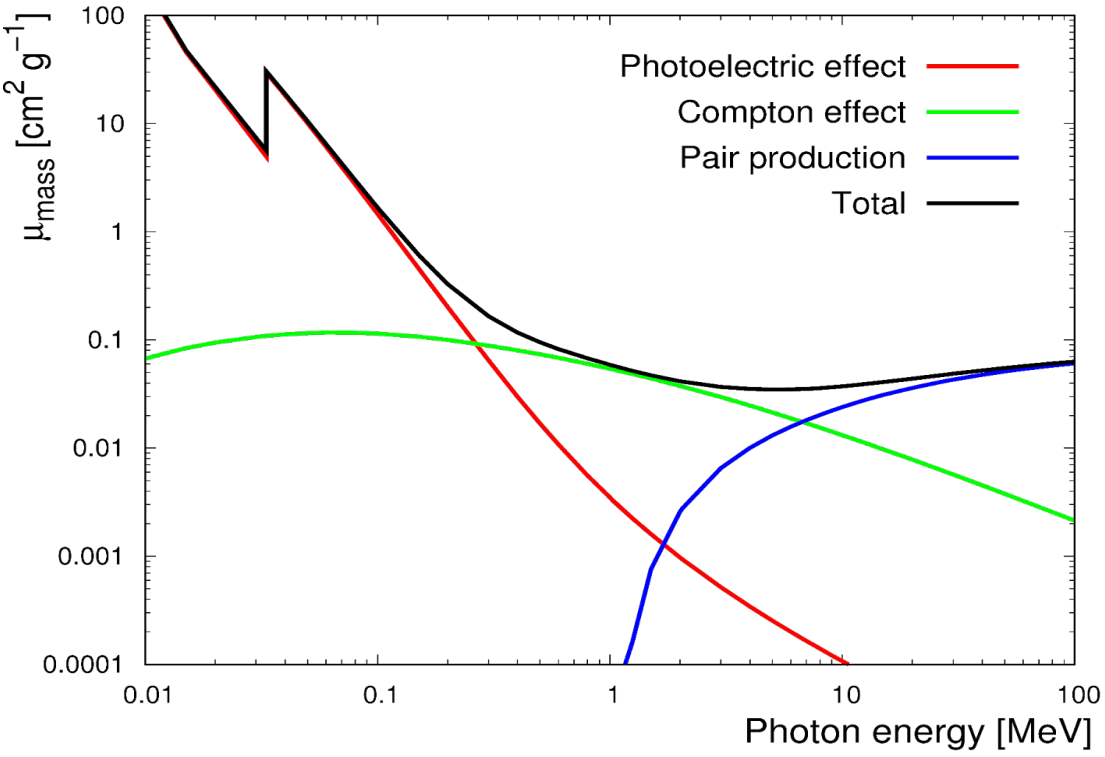

Figure 2.5: Total mass attenuation coefficient of NaI as a function of energy with contributions from photoelectric effect, Compton effect and pair production. The regions in which each interaction is dominant is shown clearly. The Compton edge in the lower γ ray energy region in the photoelectric effect is also clearly visible. [25]

Figure 2.5 shows that the photoelectric absorption dominates in lower energies, around 0.01MeV to 0.3MeV, and the material more readily absorbs photons in this energy range. For higher energy photons, around 8MeV to 100MeV, pair production starts to dominate. In between these energy ranges the Compton effect is the main contributor to total attenuation.

2.3 γ ray Spectroscopy

The three γ ray-matter interactions discussed above all contribute to the measurements taken by γ ray detectors. These different interactions each give rise to distinctive features seen in γ ray spectrums. Below is a typical γ ray spectrum from a medium-high energy source.

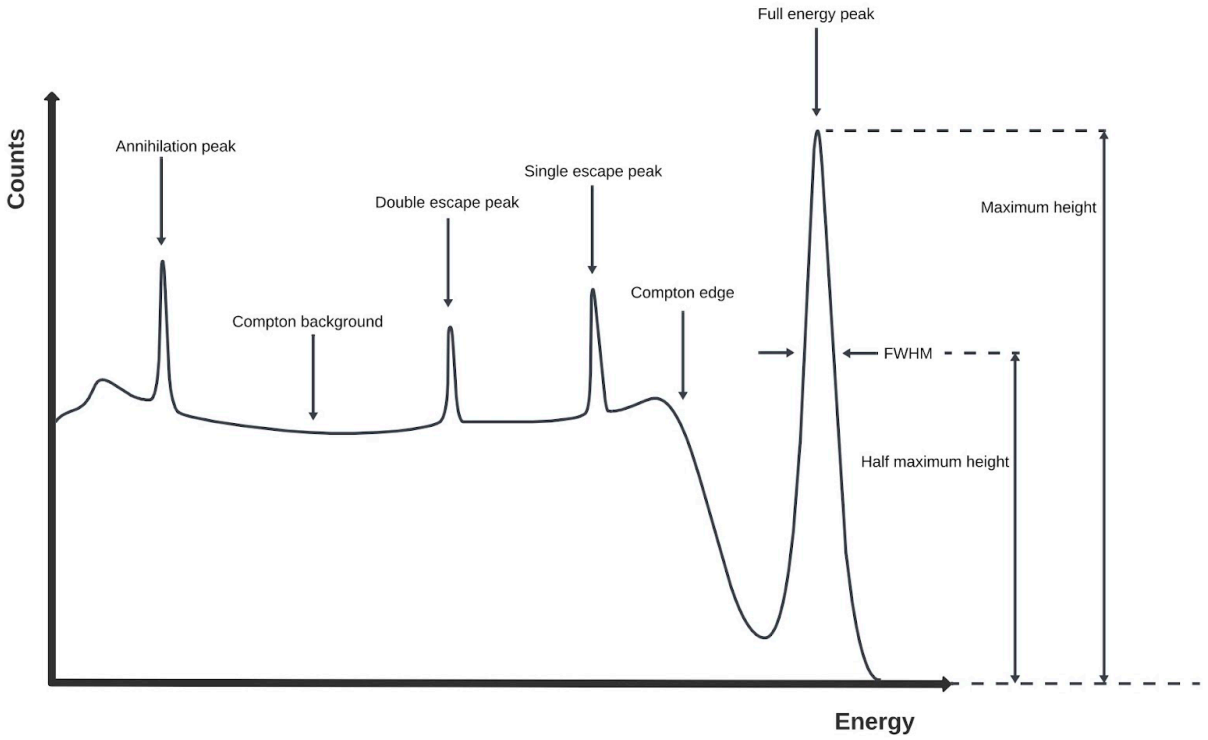

Figure 2.6: A typical γ ray spectrum for medium-high energy (over 1.022MeV) γ rays. The main features commonly observed for γ ray spectrograms are annotated.

The most prominent feature on the spectrum is the full energy peak which corresponds to the full energy of each γ ray photon from a particular source. In this case, the full energy from the γ rays are deposited into the detector. This can happen directly in one photoelectric interaction or can occur through multiple events, for example through some Compton scattering and then photoelectric absorption. Despite these interactions taking place one after another the time difference between them is effectively zero compared to

the time resolution of the detector. This means in the ideal scenario that the lower energy photons produced from interactions of one γ ray photon are detected as one pulse. The energy peak can be broadened by a number of factors including inefficiencies of the detector or recoil electrons from Compton scattering losing energy. The detector's energy resolution is determined by measuring the full width at half the height of the peak (FWHM) as a percentage of the centroid of the peak. The peak to background ratio is often used to describe the intensity of the peak relative to the intensity of the background.

Before the full energy peak, there is a large diffuse area of counts called the Compton background, as the name suggests this arises due to the Compton scattering interaction. As discussed, energy deposited by the γ ray photon is dependent on the angle at which it scatters. Some of these Compton scattered photons will then escape the detector, losing the portion of energy that it still had remaining. This takes energy away from the full γ ray value resulting in a continuum of energies being detected below and almost up to the full energy peak, with the backscatter case depositing a large fraction of the γ ray energy. The edge where this region drops off just before the full energy peak is called the Compton edge.

Within the Compton background area there are three peaks, the higher energy two are the double and single escape peaks. These two peaks are caused by pair production taking place within the detector. In the case of the single escape peak, after the positron from the pair production has annihilated, one of the resulting 511KeV photons escapes the detector and the rest of the energy from the initial γ ray photon is collected by the detector. This results in a peak of 511KeV lower than that of the full energy peak. In the case of the double escape peak, both of the annihilation photons escape the detector which drops the detected energy in this case by another 511KeV.

Finally, the lowest energy peak, the annihilation peak, sits at 511KeV and is due to single photons emitted by pair production. These pair production interactions have to occur outside the detector for this peak to be present as energy from the electron or the second

annihilation photon would increase the energy of the peak to the levels of the double and single escape peaks discussed above.

2.4 Scintillating Materials

To measure radioactivity and detect γ rays, the individual γ ray photons need to be counted and measured. There are several approaches to this, one of the most common, and the one used in this project, is detection via scintillation. This section looks at the properties of scintillators generally, then discusses the two main types, organic, and inorganic. The specifics of inorganic scintillators are then further explored in section 2.4.3.

2.4.1 Characteristics of Scintillators

When evaluating the performance of scintillators there are several important characteristics which are outlined below.

Scintillating materials used in γ ray detectors are assessed on several characteristics that make them more or less appropriate for different applications. The first characteristic is its light yield. This is one of the most important factors for a scintillating material, this is measured by the number of photons produced per unit of energy deposited in the material. The light yield (LY) of a material is given in Eq. 2.9. Dependant on the scintillator the LY can typically be in the range of 10^3-10^5.

$$LY = \frac{N_{scintillated\ photon}}{E_\gamma} \tag{2.9}$$

LY is governed by the number of electron-hole pairs that are produced by the γ rays interacting with the material. For an inorganic scintillator this is determined by the band gap E_b of the material. The greater the band gap the lower the light yield will be as more energy is required to excite electrons from the valence band.

The second characteristic is response time. This refers to the time taken for the scintillator to release scintillation photon after the interaction of a γ ray photon. This parameter is controlled by the decay time of the material, in the case of inorganic scintillators this is

the time in which the excited electrons decays back down to the valence band via photon emission.

The self-absorption of light is the third important characteristic of scintillators. This refers to the amount of scintillated light that is reabsorbed by the scintillator. If this property is high, then the response time of the scintillator can be negatively affected due to reemission.

The last characteristic is the energy resolution. The intrinsic energy resolution of a scintillator is determined by the light output of the scintillator as well as the proportionality of the response. The light yield is an intrinsic property of a material but other factors such as inhomogeneities can cause areas of differing light yield, further reducing the proportionality.

2.4.2 Organic Scintillators

There are two main types of scintillators used for γ ray detection, these are organic and inorganic scintillators. The first type, organic scintillators, can be split in to 3 subcategories: organic crystal, organic liquid and plastic. These organic scintillators are made up of aromatic compounds, meaning they contain a benzene ring. It is common for the aromatic matrix that makes up these compounds to not have good light emission properties, so a fluorescent dye is sometimes added. The dye is added to only a concentration of 1-5% [26] meaning most of the ionisation by γ rays is on the aromatic mix. If the energy levels of the dye and the aromatic mix are well matched there can be a rapid transfer of energy from the mix to the dye which is the cause of most of the scintillated photons observed.

The three different types of organic scintillator are discussed individually below.

The first type is organic crystals. These crystals are grown from a solution or melt of the organic aromatic compound and additional dyes. It is very difficult to grow such crystals

larger than a couple of inches and they suffer from an efficiency dependence on their orientation. This means their energy resolution is reduced for radiation that produces tracks through a large range of angles in the crystals.

The second type is liquid organic scintillators. These are produced by dissolving an organic scintillator in a solvent and often have a component added that shifts the wavelength to the desired range. This is done to reduce reabsorption by improving the transparency of the material to the scintillated light. The liquid scintillator has an advantage over other types that have a solid structure that can be damaged by high-energy radiation, making the liquid scintillator more resilient to this degradation.

The third and final type is plastic scintillators. Similarly to liquid scintillators, these are produced by dissolving an organic scintillator in a solvent, but for plastic scintillators, this solution is then polymerized to form a solid. Plastic scintillators can be easily formed and are relatively cheap making them highly versatile. Both plastic and liquid scintillators are well suited to large-volume detectors due to their cost and scalability. Plastic scintillators, however, are not very radiation resistant meaning they can degrade quicker than other scintillators and this limits their applications.

2.4.3 Inorganic Scintillators

The second category of scintillator, inorganic scintillators, is the focus of this project, specifically, inorganic crystal scintillators. Inorganic crystals are often made of ionic crystals with a high effective atomic number (Z_{eff}). This makes them good candidates for ray spectroscopy, Eq. 2.4 shows that for photoelectric absorption $\tau \propto Z^{3-4}$. The scintillation process of these materials can be split into three main stages, absorption/multiplication, charge carrier migration, and relaxation/emission.

The first stage, absorption/multiplication, occurs when a high energy particle enters the scintillator, and its energy is partially or fully absorbed. This creates an electron hole pair from the inner shell of the scintillator. This primary electron and hole then multiply through interacting with other electrons in the scintillator, creating secondary x-rays and other free electrons, through electron-electron scattering and auger processes. Once the energies of the free electrons become lower than the ionisation energy, they thermalise to the lowest energy states in the conduction bands and the holes occupy the highest states in the valence band. The second stage, charge carrier migration, can then take place. Due to the site of excitation usually not being the same as the site of relaxation the electrons and holes need to migrate to luminescence centres. These luminescence centres are created by either extrinsic factors, doping, or intrinsic factors like lattice defects. Once this has happened, the final stage, relaxation/emission, can occur. The excited electrons release their energy through the emission of a photon and return to the valence band.

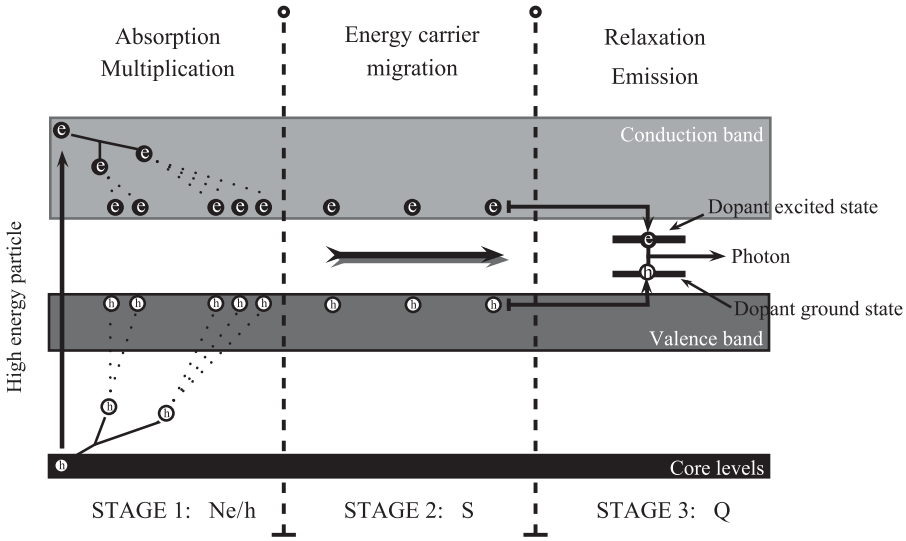

Figure 2.7: Diagram showing the 3-stage scintillation process in inorganic crystal scintillators. Holes are represented by white circles with an h inside and electrons by black circles with an e inside. [27]

As Figure 2.7 shows, inorganic crystal scintillators often have impurities added to the crystal structure in a process called doping. This doping introduces new energy levels in between the conduction band and the valence band of the pure crystal, shown in Figure

2.7 as dopant states. These dopant states increase the number of photons produced in the visible light regime by reducing the band gap and thus reducing scintillated photon energy. They also help to avoid self-absorption of photons. Without these dopant states the photons emitted due to the transition of electrons from the conduction band to the valence band would exactly match the band gap in the material and would very effectively be reabsorbed.

2.5 Silicon Photomultipliers

Once gamma rays have interacted with the scintillator volume in the detector the scintillated light produced needs to be collected and measured. This project uses Silicon Photomultipliers (SiPMs) to do this. SiPMs are semiconductor devices that when hit by a photon produce a current signal that can be tens of nanoseconds long. SiPMs are devices with a gain and can produce 10^5 electrons from a single photon hitting the surface.

2.5.1 SiPM construction and operation

SiPMs are made up of many silicon diodes that are sensitive to light, called avalanche photodiodes (APDs). These operate on the same principle as other silicon diodes, using a p-type and n-type semiconductor junction. The p-type material has been doped with an element with fewer electrons in its valence band than silicon giving an excess of positive holes or donor sites. The n-type material has been doped with an element with more electrons in its valence level giving the material an excess of negative electrons, donor electrons. When p-type and n-type materials form a junction The positive holes from P-type material attract the electrons from N-type material leaving behind holes in the n-type. This process is called diffusion and creates a region in the middle of the junction where there are no holes in the valence band or electrons in the valence band. This region is therefore depleted of charge carriers and is called the depletion region. The diffusion of the electrons from the n-type also creates an area of negative charge in the p-type and an area of positive charge in the n-type. These charged regions give rise to a potential across the junction.

When a power supply is connected across the pn junction, with the anode connected to the p-type and the cathode to the n-type, and a positive potential supplied, the width of the pn junction shrinks. This is due to the negative electrons being repelled from the cathode and the positive holes being repelled from the anode. Once the applied potential is greater than the opposing potential of the depletion region, called the potential barrier, charge carriers will be able to flow. This mode of operation is called forward bias. If a

negative potential is supplied (negative supplied to the p-type material and positive supplied to the n-type material) the diode is in reverse bias mode. This causes the depletion region to expand as the free charge carriers are pushed away from the junction by the negative potential, making it very hard for charge carriers to flow. Only a small amount of current will be observed, the saturation current. As the supplied voltage increases the diodes resistance eventually breaks down and a large amount of current is able to flow. This primarily occurs through two mechanism, Zenner breakdown and avalanche breakdown. Zenner breakdown occurs in the electric field induced by the voltage supply, it causes the gap between the valence band of the P-type and the conduction band of the N-type in the depletion region to reduce. This happens when the coulomb field in the diode is around 10^6V/cm [28]. Electrons are then able to tunnel from the P-type to the N-type via quantum tunnelling.

The second mechanism, avalanche breakdown, is the basis for the avalanche photodiode (APD) which make up SiPMs. Avalanche breakdown is caused by electrons that are free being accelerated by the applied electric field and colliding with lattice atoms in the diode. This collision excites the electron from the valence band to the conduction band where it is then accelerated by the electric field. This continues in a chain of events leading to an avalanche of electrons. For this to occur the maximum field strength must be $>5\times10^5$V/cm [28]. The avalanche breakdown voltage is the voltage required for free electrons to knock out other electrons, this mode of operation is called Geiger mode.

In APDs the free electron that starts the advances is initially excited by absorption of a photon. A current, I, will then flow through a quenching resistor connected in series with the APD. The quenching resistor reduces the voltage at the diode to close to the breakdown voltage. This neutralises the residual charge and stops the avalanche enabling the APD to detect another photon. The quenching resistor and APD together are called a micro cell. An SiPM is constructed of an array of these microcells, all connected in parallel. This means all microcells are biased with the same voltage and produce the

same output for a single photon. The output of the SiPM is therefore proportional to the number of photons detected.

2.5.2 SiPM Nonlinear Response

In an ideal SiPM the output would be directly proportional to the number of photons detected, however, in the real world this is not the case. The reason for this is due to SiPMs having a finite number of microcells. When the total number of photons (N_{Photon}) incident on the SiPM at one moment is significantly lower than the total number of cells (N_{Total}), the output can be expected to be almost directly proportional to the number of photons. However, when the number of incident photons is higher, the output of the SiPM becomes nonlinear. This is due to the randomness of the spread of photons, causing some microcells to be hit by multiple photons. These microcells that have multiple photon incident on them will produce the same avalanche as those with only a single photon. This is shown below in Eq. 2.10.

$$N_{Firedcells} = N_{Total}\left(1 - e^{\frac{-N_{Photon}PDE}{N_{Total}}}\right) \tag{2.10}$$

PDE is the photon detection efficiency of the SiPM. This also shows the logical limit of the SiPM output to be the total number of cells, this point is called saturation.

This model looks only at the case of photons arriving simultaneously to the SiPM. In reality, photons will be hitting the SiPM over a period of time. If a photon hits a microcell that is in the middle of an avalanche the photon will not be registered as is descripted above. Avalanches last less than a nano second, however the microcell has not fully recovered back to its full operating state after this. The voltage of diode V, is dependent on the current flowing through the quenching resistor I and its resistance R_q. This is shown below in Eq. 2.11. Where V_{op} is the operating volage of the APD and V_{op} is the operational overvoltage that the SiPM is biased to.

$$\mathrm{V} = V_{op} - I(t)R_q \tag{2.11}$$

When an avalanche takes place within an APD the overvoltage can be assumed to be reduced to 0. This gives Eq. 2.12 [29]

$$\mathrm{I(t)} = \frac{V_{op}}{R_q} \exp\left(-\frac{t}{\tau_{rec}}\right) \tag{2.12}$$

The recovery time of the microcell τ_{rec} or the time constant, is approximately $R_q C_d$, where C_d is the capacitance of the diode.

Eq. 2.12 in conjunction with Eq. 2.11 gives.

$$\mathrm{V(t)} = V_{op}\left(1 - \exp\left(-\frac{t}{\tau_{rec}}\right)\right) \tag{2.13}$$

Eq. 2.13 shows the voltage of APD as a function of time after an avalanche. If another photon were to hit the microcell before $\mathrm{V} = V_{op}$ another avalanche would be triggered but this time with a lower overvoltage driving it. This would result in a lower gain and a lower signal output for that event.

2.5.2 Other SiPM limitations

Another issue experienced by SiPMs is that of dark counts. This is where thermally excited electrons enter the APD and are accelerated by the high field, causing an avalanche. The likelihood of this phenomena can be reduced by keeping the SiPM from getting too hot which could result in more thermally excited electrons and thus more dark counts.

When an avalanche breakdown occurs in an APD there are on average 3 photons emitted for every 10^5 electrons, from the silicon [30]. These photons have an energy greater than

1.14eV, corresponding to the band gap of silicon. This can cause nearby microcells to fire as a result of the emitted photons, causing a crosstalk avalanche. The likelihood of crosstalk avalanches can be reduced by operating the SiPM at a lower gain to reduce the number of electrons produced per avalanche.

3 Experimental Setup

3.1 Canned Scintillator Detector

This section will go through the experimental setup and design of the prototype detector housing as well as the materials used. The process of constructing the detector is also discussed below. The detector design presented in this section is the prototype design for use in the HYPATIA array as discussed in section 1.

3.1.1 Scintillator, material and SiPM choices

The scintillator crystals chosen for this project were NaI(Tl), from Epic Crystals [31], as opposed to the CeBr3 which is intended for the scintillator detectors in the barrel of the HYPATIA array. The primary reason for this choice was the cost, NaI(Tl) crystals are much less expensive than the CeBr3 crystals intended for final use. Both crystals are hygroscopic so would need identical preparation and sealing to prevent degradation. NaI(Tl) is also a very well tested and documented scintillator allowing for comparison with other detectors to assess both the housing and methods of light proofing and SiPM coupling.

The crystals had to be independently wrapped using a material which is highly reflective to the scintillated light. This increases the number of scintillated photons that would reach the SiPM coupled to the crystal. It also reduces optical crosstalk which is where scintillated photons from one crystal enter a second crystal and are detected by the SiPM coupled to the secondary crystal. NaI(Tl) has a maximum scintillation light wavelength of 415nm [32]. Polytetrafluorethylene (PTFE) was selected to be the wrapping material as it is highly reflective in this range. It has been measured to have a >95% reflectance at 440nm if the thickness is >0.5mm [33].

The SiPMs used in this experiment were 6x6mm s14160-6050HS from Hamamatsu. Four of these SiPM units were mounted in a 2x2 array onto a PCB produced by the York PET Electronics Workshop which connected the four SiPMs in series with a single signal output and single bias. The PCBs with the 2x2 arrays mounted measured 13.0±0.1mm by 13.0±0.1mm. To mount these arrays to the crystals optical grease EJ-550 [34] was used as a coupling agent. The optical grease creates a thin layer between the crystal and SiPM, filling any imperfections and airgaps which would have refractive index of close to 1 and would limit the angles at which γ rays can leave the crystal and enter the SiPM. The refractive indexes of the SiPMs, NaI(Tl), and optical grease were 1.57 [35], 1.85 [31], and 1.46 [34] respectively.

3.1.2 Crystal Wrapping

The process of wrapping the crystals and hermetically sealing them in the aluminium housing was done in a Nitrogen environment. This was done due to the Hygroscopic nature of NaI(Tl). A glove box was used to facilitate this, enabling work to be done on the crystals in >0.05ppm H_2O conditions.

Within the York Nuclear Physics group extensive testing has been done on the optimal wrapping of scintillator crystals and the result of this is the York standard which is to wrap using this 0.2mm tape with a minimum of 8 layers (1.6mm total thickness). This standard was upheld in this experiment and used 1 mm thick PTFE sheets to cover the ends of the crystals, ensuring the 1 mm minimum thickness.

SiPM was fitted on the one end of the crystal on one of the smallest faces of the cuboid This is shown in Figure 3.1. This was done for two reasons: SiPM efficiency and easy access when the crystals were loaded into the housing. Mounting the SiPM to one end makes it easier for it to be hit by scintillated photons that are reflecting off the PTFE wrap on the outside of the crystal. One of the PTFE sheet end caps had a 13.2x13.2mm window

cut into the centre of it to fit an SiPM array. It was found that a tolerance of +0.2mm gave the best fit around the SiPM without deforming or stretching the PTFE. A laser cutter was used to ensure a tight fit and reduce any light loss through the gap between the PTFE and the SiPM.

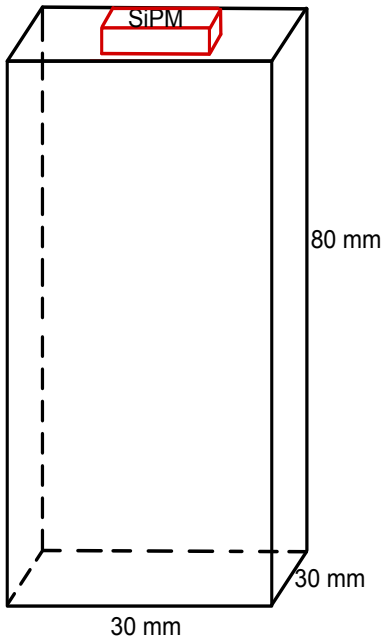

Figure 3.1: Diagram showing the SiPM (red) mounting position on the NaI(Tl) crystals (left) and a photograph on the SiPM being test fitted into the PTFE sheet window (right). This photograph was taken during a test fitting, the crystal and SiPM were later warped using the described method.

The PTFE sheet cut-out was first placed on the short end of the crystal and the SiPM was mounted with the optical grease. The minimum amount of grease was used to ensure full coverage and minimise and being pushed out from under the SiPM. It was applied using a small plastic spatula, around 5mm wide to avoid scratching the SiPM or applying too much. If the grease contacts the PTFE, it reduces its reflective properties and leads to losses. The crystals were then wrapped using the following method:

The second un-cut PTFE sheeting square was placed on the bottom and a layer of PTFE tape was wrapped around the crystal to secure the top and bottom PTFE sheet caps. This took 4 passes to cover the 4 surfaces covered by that axis.
The crystal was then rotated 90 degrees and another layer of PTFE tape was wrapped; this was also along the long sides of the crystal. This created a layer of 0.2mm thick PTFE on the long sides of the crystal and a 1.2mm thick layer on the ends.
The remaining 7 layers were applied by wrapping the PTFE tape perpendicular to the long sides of the crystal. After each layer was completed the direction of wrapping was reversed without breaking the tape.

After wrapping the average thickness of the crystals plus PTFE was 33mm. During the wrapping process, some damage was sustained by two of the crystals. The first was damaged much more severely which is shown in figure 3.2 below. The crystal appeared to still be usable, and the degradation caused is discussed in chapter 5. The second, shown in Figure 3.3, only sustained minor damage in the same incident. To prevent any further damage a felt sheet was added to the glove box where the crystals were being wrapped to reduce any potential impact with the metal box.

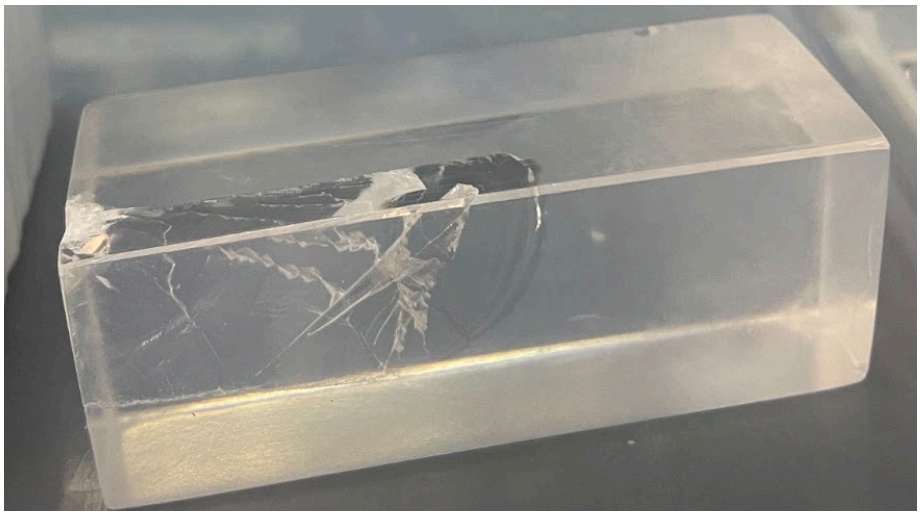

Figure 3.2: Crystal 2 in the glove box after an incident that caused damage to it and Crystal 4. Large cracks can be seen in the upper left quadrant.

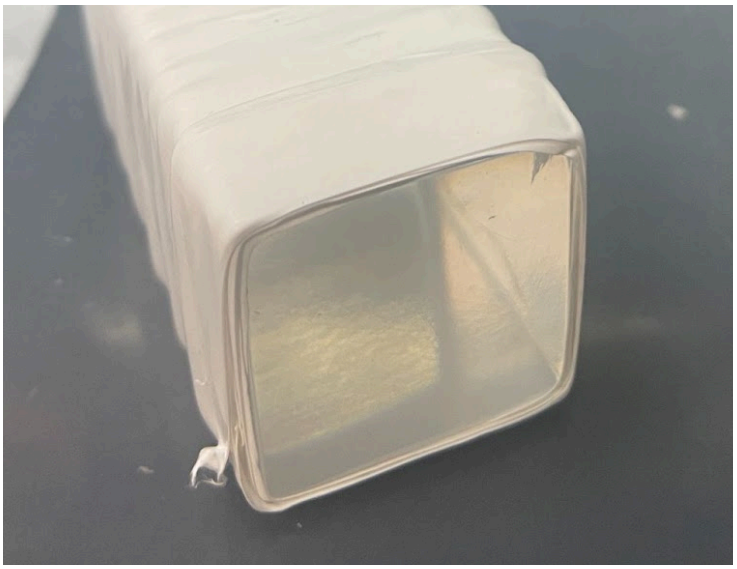

Figure 3.3: Crystal 4 wrapped on the sides with PTFE tape and the end cap removed. A small crack can be seen in the top right corner of the end face.

3.1.3 Can Design

The design of the detector housing had to address several requirements for use in the HYPATIA array. It needed to be large enough to house 4 30x30x80mm crystals (NaI(Tl) in this project) and the additional size increase caused by wrapping, as well as be hermetically sealed so no moisture would contact the hygroscopic crystals. The detector also needed to fit in the array shown in Figure 1.2 and limit the spacing between each detector unit. As well as this the housing needed to be as thin as possible to maintain efficiency and not lose incoming γ rays to scattering off the housing. The material chosen for the housing was aluminium as it has a low atomic number (Z). As shown in Eq. 2.4, Eq. 2.6, and Eq. 2.8 lower Z number materials have a lower photoelectric absorption, pair production, and Compton scattering probability, resulting in greater efficiency of the detector. The can was machined from a solid block of aluminium so that no joints were required in fabrication, reducing potential weak points. The design schematic for the housing is shown below in Figure 3.4.

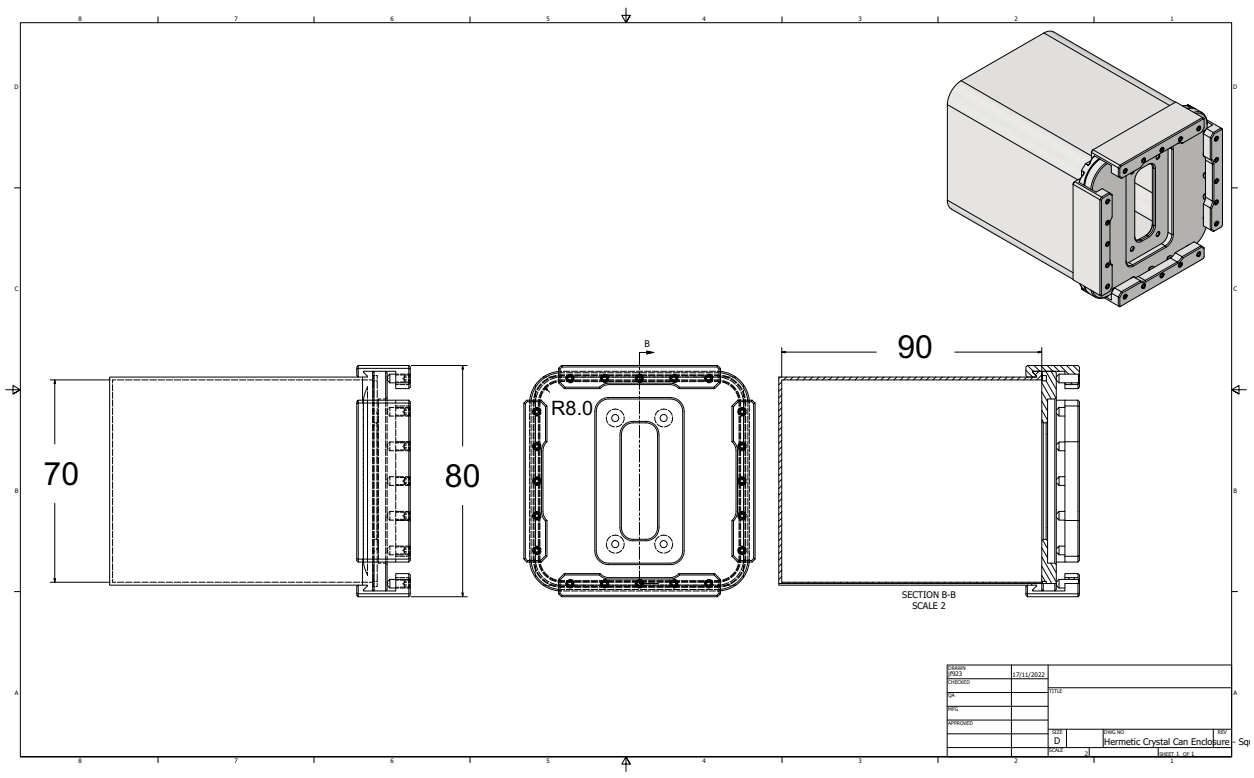

Figure 3.4: Schematic of aluminium housing for the scintillator detector. The side views are shown by the left and right line diagrams, with the front view in the centre. The width, length and height have been labelled on the line diagrams as well as the internal curvature. This design and drawing were supplied by the York PET machine workshop.

Once the dimensions and specifications of the aluminium housing were finalised it was machined. The finished product had a thickness of 0.9±0.1mm. This thickness was the thinnest the housing could be made in house while maintaining structural integrity. An image of the fully disassembled housing is shown in Figure 3.5. The housing uses a clamping system with rubber O-ring to create an airtight seal between the main body and the lid. Four aluminium pieces hook over the lid and the lip of the body and are tightened down by five screws on each side. A close-up view of this system is shown in Figure 3.6.

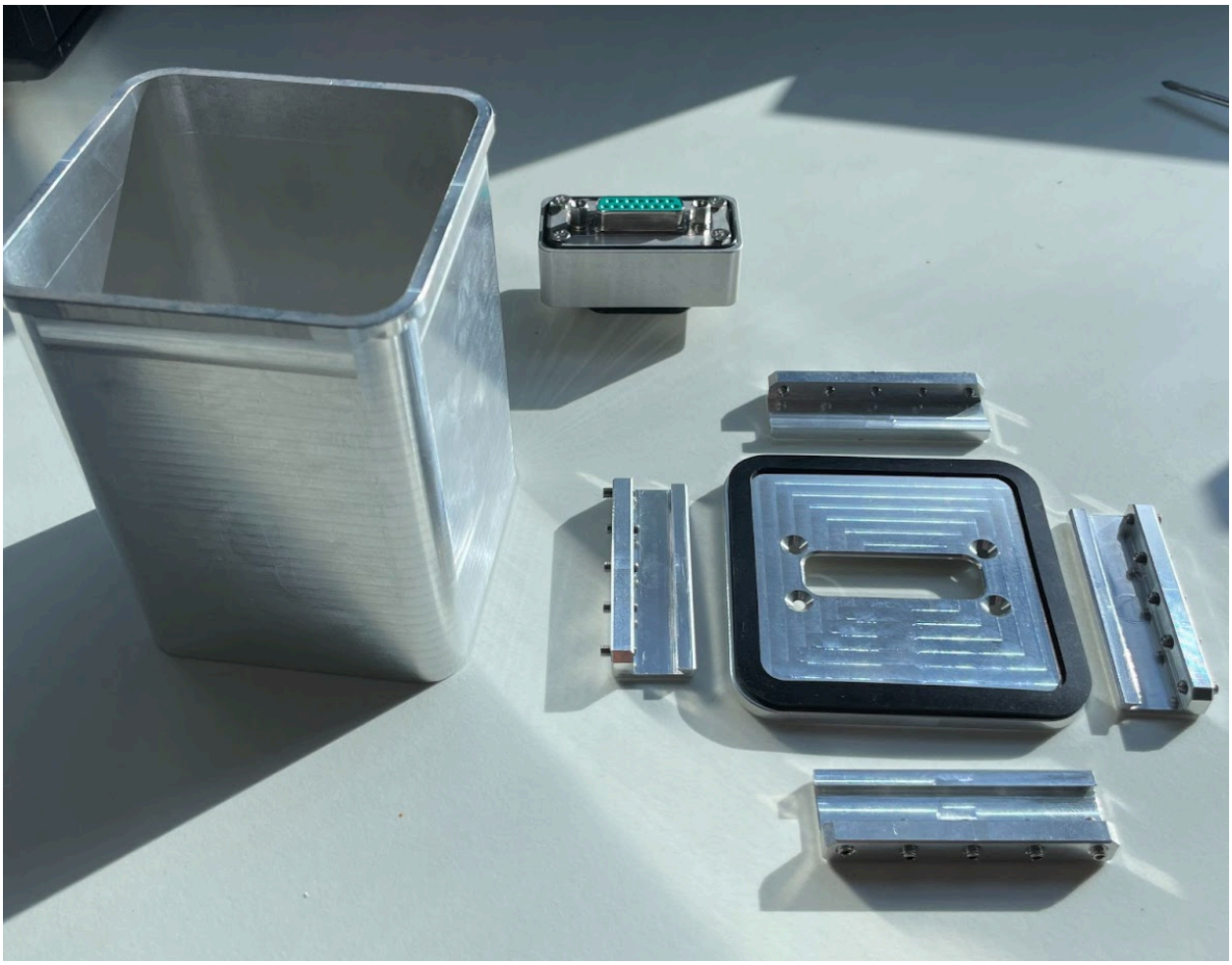

Figure 3.5: Fully disassembled aluminium housing**.** On the right there is the lid with the O-ring seated in its groove as well as all four clamps laid on each side of the lid. At the back there is the passthrough connector which mounts to the lid.

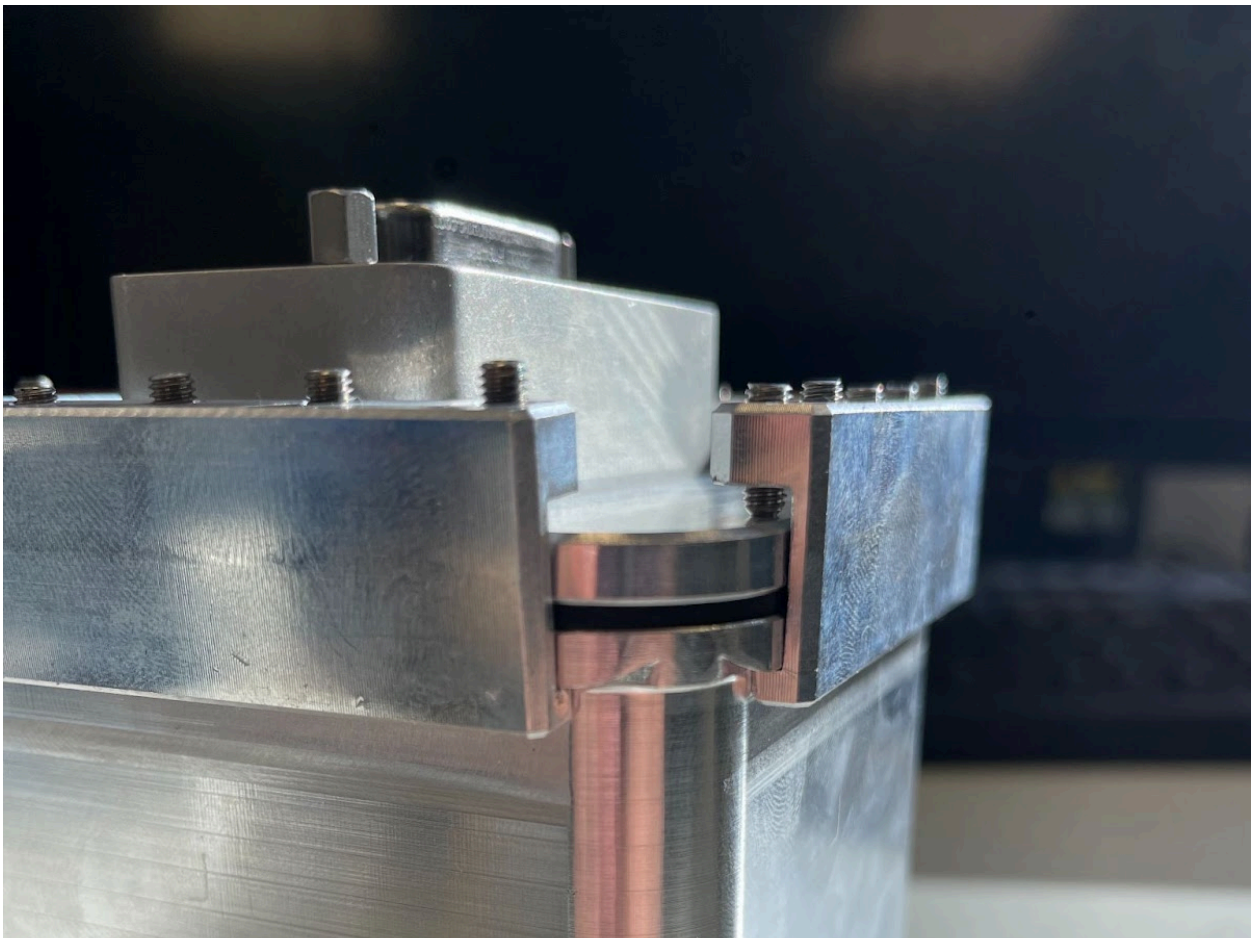

Figure 3.6: Close-up view of the clamping system. The six clamping screws have been tightened on all sides to secure the lid. The overhang of the sides by the clamping mechanism can been clearly seen.

Before the metal housing was machined, the entire assembly, including crystals wrapped in PTFE tape 1.6mm thick, was modelled using CAD software to ensure the fitment of all parts would be good. The side view looking at a slice through the 3D assembly is shown below in Figure 3.7.

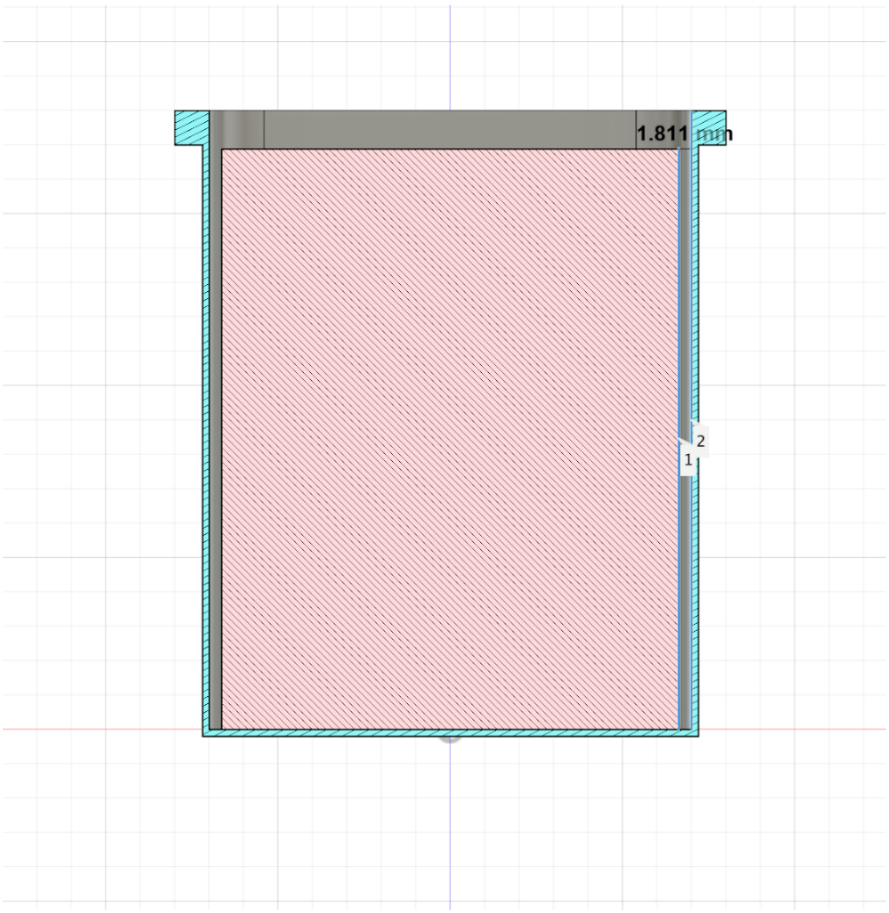

Figure 3.7: Screenshot taken of a slice through a 3D assembly made in Fusion 360. The assembly shows the aluminium housing (grey with sliced section shown in blue) and a dummy crystal (pink). The dummy represented an estimate of the combined size of all four NaI(Tl) crystals with PTFE wrapping. The distance between the side of the housing and the crystal has been measured as 1.811mm in the software and labelled.

This 3D analysis showed a gap of around 1.811mm on each side of the crystal. This would result in the crystals having a combined 3.622mm of room to move in each axis. This raised concerns that the crystals could rattle around inside the can, causing damage. The solution was to 3D print a thin 1mm spacer that would remove this excess space. The 3D printed piece was designed to use as little material as possible so as to reduce its impact on the efficiency of the crystals. The design is shown below in Figure 3.8. The

other main factor to consider was the properties of the material under vacuum and its moisture retention. The piece would have to be put under a vacuum to put it into the nitrogen filled glove box that the crystals would be wrapped and sealed in. 3D printed pieces often suffer from deformation caused by internally trapped gas escaping when subjected to vacuum. Due to the thickness of the piece and the overall low mass, there was a very low risk of this occurring.

The other concern was that of moisture retention, the material had to be carefully selected to minimise this. It was found that Nylon 12 (PA12) had very similar outgassing and moisture retention characteristics to those of PTFE (Teflon) [36]. As PTFE tape is very commonly used to wrap these types of hygroscopic crystals this was a good choice of material. The piece was then printed in PA12, and a photograph of the finished piece is shown in Figure 3.9.

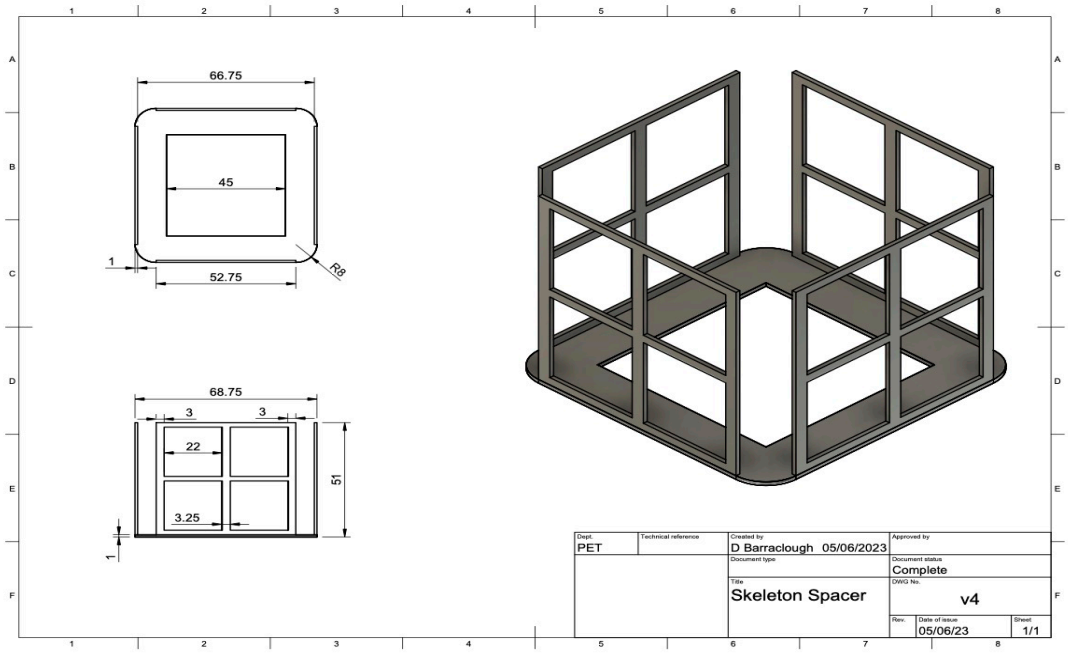

Figure 3.8: Drawing of spacer insert designed in Fusion 360. The top view and side view are shown on the left with dimensions labelled. The piece consists of 5 elements, printed separately.

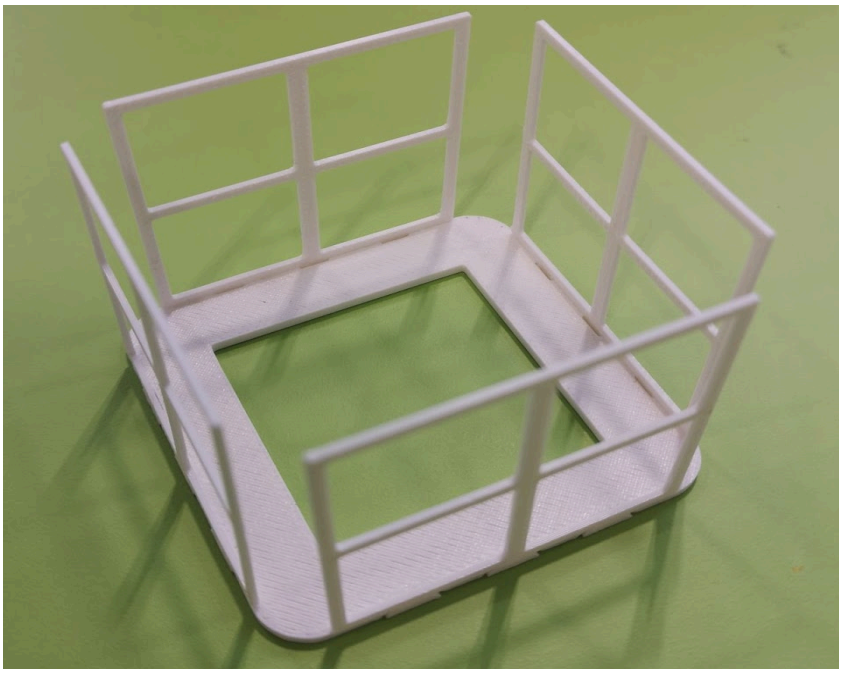

Figure 3.9: Photograph of finished 3D printed, PA12 spacer. The four sides have been clipped into the base using 3 friction fit dovetail joints on each side of the base.

3.1.4 Passthrough Connector

To get data from the detector and process the signals from the SiPMs there needed to be a passthrough connector to interface between the interior of the detector and the outside. To do this a 15-pin connector was produced, an image of this is shown below in Figure 3.10. The connector needed to also create an airtight seal between itself and the lid of the detector. This was once again achieved using an O-ring and the whole connector was tightened down to the lid via 4 screws. Figure 3.8 shows the countersunk holes in the lid that were used to attach the passthrough connector. Table 1 shows the pin connections of the connector.

Figure 3.10: 15-pin passthrough connector viewed from the internal side. The rubber O-ring can be seen which creates the airtight seal. The metal exterior that provided the hermetic seal for the connector was produced by the York University Machine Workshop.

Table 1: Table showing the pin connections for the 15-pin passthrough connector used to connect the SiPM arrays on the crystals to the bias supply and digitiser.

Pin	Function
1	Temperature probe signal out
2	Temperature probe 5V in
3	Temperature probe ground
4	n/a
5	cathode 0
6	cathode 1
7	cathode 2
8	cathode 3
9	Anode 0
10	n/a
11	Anode 1
12	n/a
13	Anode 2
14	n/a
15	Anode 3

The anode pins are spaced apart to reduce any noise or interference from other channels. The cathodes did not need to be isolated like this as the detector used 4 identical SiPM arrays so they were all be biased with the same voltage from the same source.

Once the passthrough connector was mounted to the lid the detector was assembled in a nitrogen environment inside a glove box. The four crystals were inserted into the housing with extra strands of PTFE tape placed underneath to be used for future removal. This is shown in Figure 3.11 below. The PA12 spacer was not used as the dimensions of

the wrapped crystal were thicker than had been anticipated. This may be due to unintentional overlapping of PTFE layers caused by doubling back at the ends of the crystals to add new single layers. The four crystals labelled 1,2,3 and 4 starting in the top left of Figure 3.11 and finishing in the bottom right. Figure 3.12 shows a sketch of this layout.

Figure 3.11: Wrapped crystal placed inside the aluminium housing before being wired to the connector and hermetically sealed. Strands of PTFE can be seen looped underneath the crystals for easier extraction.

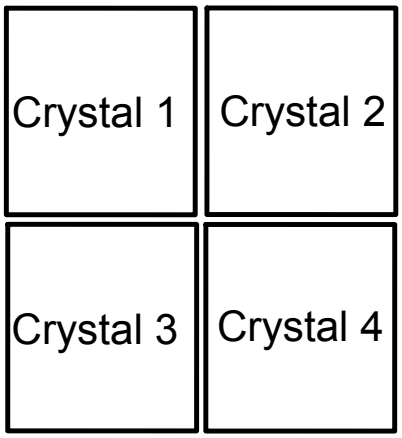

Figure 3.12: Layout of the crystals inside the detector housing when viewed from the end. The orientation is the same as that in Figure 3.11.

3.1.5 Experimental Setup

The experiential setup for testing the sealed NaI(Tl) detector used a 14 bit, 250Ms/s Caen DT725s digitiser [37] and a Caen DT5485P USB bias supply [38]. As mentioned in section 2.5 SiPMs need to be biased in the reverse direction over their breakdown voltage to operate in Geiger mode. However, having an overvoltage that is too high increases the likelihood of crosstalk events in the SiPM. This relationship is shown below in Figure 3.13. The breakdown voltage (V_{BD}) of the SiPMs used in this project was 38V and the recommended overvoltage by the manufacturer is V_{BD}+2.7V [35]. For the acquisition of data from the tests conducted two months after the sealing of the detector ,a different digitiser had to be used as the previously used model was unavailable. For this test, a 14 bit, 100M/s Caen DT5724 [39] was used. The same a Caen DT5485P bias supply was, however, used for this test supplying the same bias voltage.

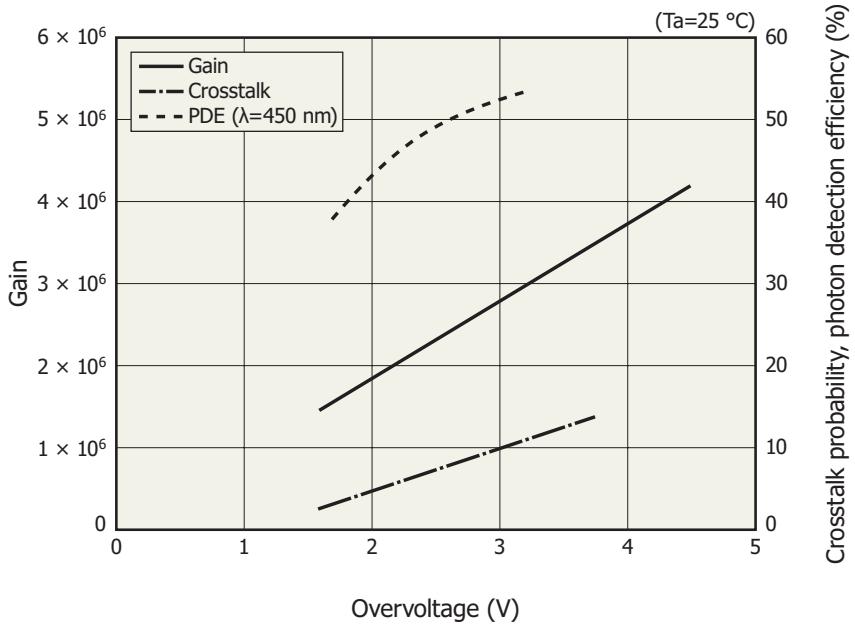

Figure 3.13: Plot showing the relationship between overvoltage and gain, crosstalk probability and PDE. The graph shows that the gain, the PDE and the crosstalk increase with overvoltage.

The bias voltage used in this experiment was chosen to be 40.5V which is a 2.5V overvoltage. Due to the time restraints of the project, testing for the optimal bias voltage with this setup was not possible so, the bias was selected based off the recommendation of the manufacturer and the York PET team.

The plotting and fitting of the data were done in the ROOT data analysis framework and used the built in fitting package [40]. For the evaluation of the performance of the detector's resolution and linearity, a Gaussian function with a linear background was fitted to determine the hight, centroid, and FWHM of peaks. The equation for this function is shown in Eq. 3.1, where a is the height of the peak, μ is the mean and the centroid of the peak, σ is the standard deviation, b is the gradient of the linear background and c is the intercept of the linear background upon which the Gaussian sits.

$$f(x) = ae^{-\frac{(x-\mu)^2}{2\sigma^2}} + bx + c \tag{3.1}$$

ROOT uses the least square method to optimise the fitted function. This method is based upon minimising the sum of the squares of the error, which is the distance between the data points and the fit. Eq.3.2 bellow shows the equation that is minimised to achieve this.

$$\chi^2 = \sum_{n=1}^{n} \frac{(y_i - f(x, \boldsymbol{a}))^2}{{\sigma_i}^2} \tag{3.2}$$

Where y_i is the ith bin of the histogram and σ_i is their uncertainty, f is a function of x and $\boldsymbol{a}$ is an array of free parameters to be fitted. The optimal parameters of the fit are determined by which return the minimum χ^2. The errors in the parameters are generated using information provided by the curvature of the function at the minimum.

3.2 Microcontroller Integrated circuit

Another aim of this project was to develop a Microcontroller integrated detection circuit. This section outlines the experimental setup and equipment used in the development of this circuit for γ ray detection. The choice of microcontroller used, and the design of the circuit are presented as well as the circuit design.

3.2.1 Arduino Microcontroller

The microcontroller used in this project was the Arduino Nano BLE 33 controller. This controller has a compact design and easy implementation, being used initially on a breadboard. The pin-out for the microcontroller is shown below in Figure 3.14.

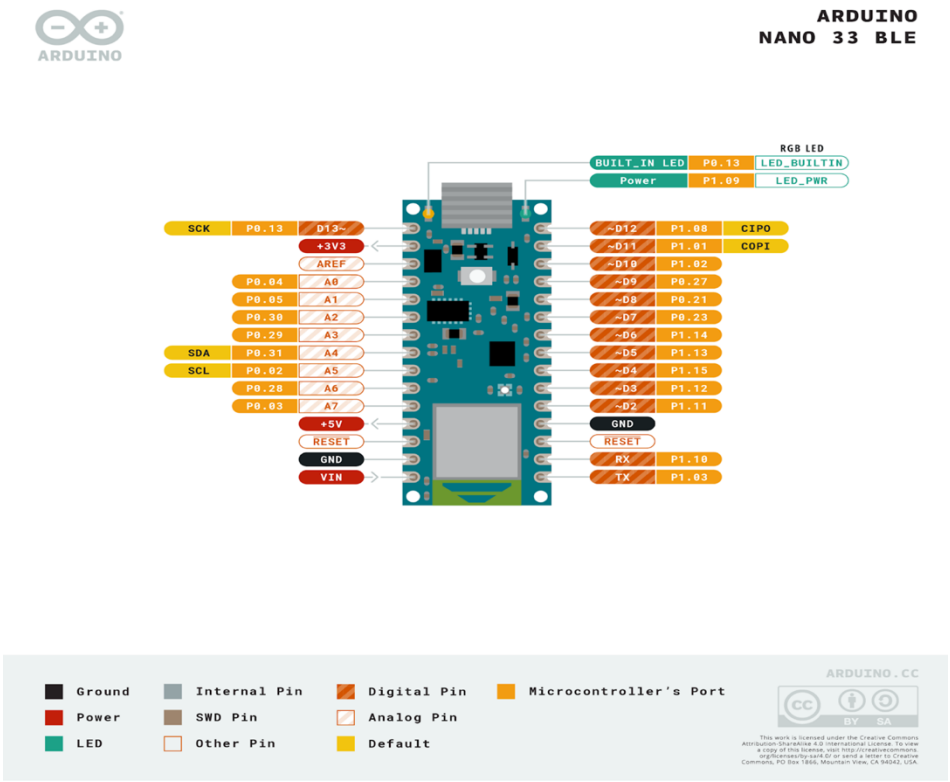

Figure 3.14: Pin-out diagram of the Arduino Nano 33 BLE Microcontroller used in this project. [41]

3.2.2 Peak Hold Circuit

The pulses produced by γ ray scintillator detectors typically range from X-Y. These pulses are too short for a microcontroller like the Arduino Nano to detect and read directly. To solve this problem, in conjunction with the microcontroller a peak-hold circuit was also used. This is a device that takes the incoming pulses and holds a constant signal that is equal in voltage to the peak of the pulse. The microcontroller is then able to read the held signal and then reset the peak-hold circuit.

The peak-hold circuit used in this experiment was designed by Tim Ayers of the York PET workshop. The design was based off the peak-hold circuit design shown below in Figure 3.15.

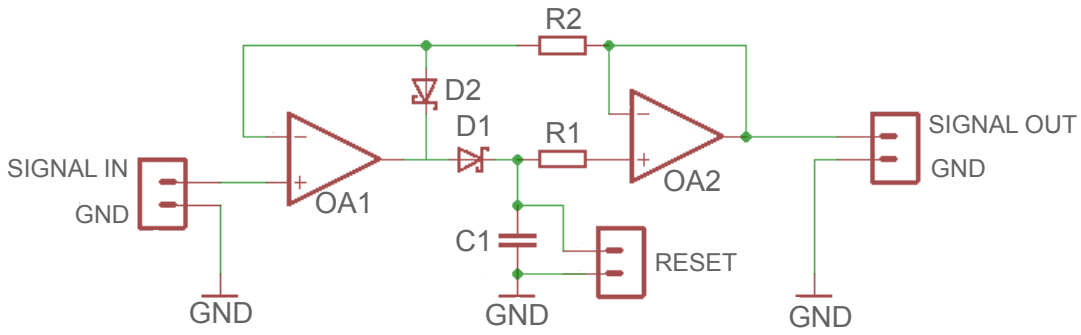

Figure 3.15: Circuit diagram of a peak-hold circuit by Physics Open Lab [42] which the peak-hold circuit for this project was based off. OA1/2 are both operational amplifiers, D1/2 are Schottky diodes, R1/R2 are 1kΩ resistors and C1 is a 10nF capacitor.

The signal input from the detector goes into the terminal on the left side of the diagram which is connected to the input operational amplifier (Op-Amp), OA1. Both Op-Amps in this circuit have a gain of zero and are used in voltage follower mode acting as a noninverting buffer. This means that the stage before the Op-Amp is not affected by the

stage after it. The signal then flows through D1, a low threshold diode, and charges up C1. In the circuit presented in the Figure above a 10nF capacitor was selected as a compromise between charge rate and discharge speed. The capacitor charges up to the peak voltage of the input signal and D1 prevents it from discharging. The input Op-Amp with the capacitor presents the held voltage on C1 as the input to the output Op-Amp, OA2. The feedback resistor R2 smooths the output signal and R1 (equal in resistance to R2) keeps the Op-Amp in follower mode. Once the signal has been read by the microcontroller C1 is discharged by the RESET terminal, in the circuit used in this project a MOSFET was used for this.

The circuit used in this project also implemented a comparator before the input to the peak-hold circuit above. This acted as a threshold to filter out lower voltage signals. The comparator uses a reference voltage to compare to the incoming pulse. If the incoming pulse is greater than the reference, the pulse is fed into the peak-hold circuit. Simultaneously a digital high signal is sent to a trigger output terminal which would alert the microcontroller to take an analogue read of the peak-hold output. This peak-hold circuit was then printed on a PCB and the pinout for the module produced is shown below. Table 2 shows the pin functions.

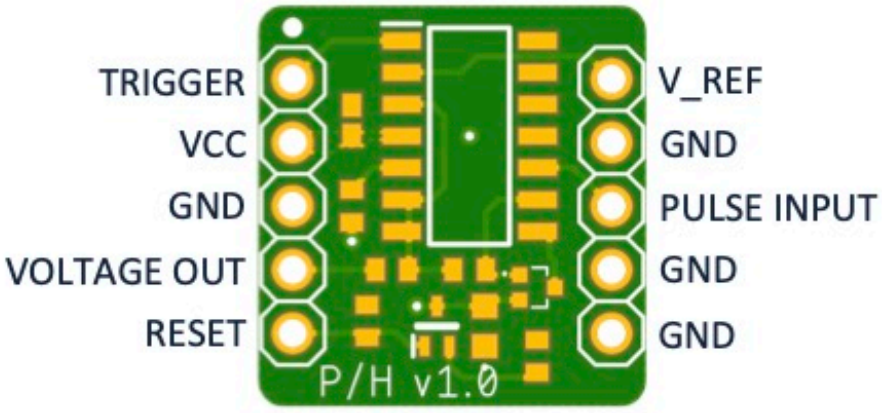

Figure 3.16: Pinout diagram of the peak-hold circuit PCB. This PCB was developed and produced by Tim Ayers of the York PET Electronics Workshop .

Table 2: Peak Hold circuit PBC pin connections corresponding to those shown in Figure 3.16. Each connection is labelled and has a descriptor of its function.

Pin	Name	Description
1	Trigger	Digital trigger output. Output is high if the pulse voltage is greater than V_REF.
2	VCC	Positive supply voltage. This must be the same voltage as the logic voltage of the Arduino.
3,6,7,9	GND	Supply and signal ground
4	Voltage Out	Analogue volt output from the Peak Hold circuit.
5	Reset	Peak Hold circuit will reset on logic HIGH input into this pin.
8	Pulse Input	Analogue pulse input.
10	V_Ref	Analogue reference voltage input for the digital trigger.

The peak-hold circuit also features a trigger pin, shown in Figure 3.15. This is controlled by a comparator, when a signal is input that is above the reference voltage a digital signal is sent to the microcontroller. This triggers the microcontroller to perform an analogue read on its input pin from the peak-hold circuit. Once the pin has been read a signal is sent to the MOSFET causing it to open and discharge the capacitor.

The speed of these read and reset cycles is determined by the length of time the microcontroller takes to perform a loop of its code. Reducing this time would enable the circuit to more accurately detect high activity sources and miss fewer pulses due to peak-hold downtime more accurately. An important step in reducing this time was the use of a

digital trigger on the peak hold circuit. Without this the microcontroller would have had to use an analogue read loop to monitor the peak hold circuit, checking if there was a pulse to record. However, using a digital read is much faster as the Arduino is only checking for a high or low signal, not the whole analogue range. So, the digital trigger allowed the Arduino code to loop faster using a digital read. This trigger pin on the peak hold circuit would go high when a pulse was being held on the capacitor.

3.2.3 DAC Controlled Threshold and Full Circuit

A main requirement of the circuit was for it to have an adjustable threshold. This was initially achieved using a potentiometer functioning as a potential divider. As the resistance of the potentiometer was changed this changed the voltage across it which would then be input to the peak hold circuit reference voltage pin. To set a user-definable threshold more easily this was replaced by a digital-to-analogue converter (DAC). The component used was an Adafruit MCP4725 [43]. The DAC would receive a 12-bit digital signal from the Arduino and convert this output to an analogue signal which was sent to the peak hold circuit as before.

The DAC, along with the peak-hold module were powered by the microcontrollers 3.3V power supply. This enabled the whole circuit to be fully powered through just a USB connection to a computer, increasing portability. With this setup it was found that the microcontroller was not able to supply the full 3.3V from its onboard power supply due to multiple components being connected. This small voltage drop resulted in a degradation of the linearity of the device at the highest energy inputs. To resolve this, a calibration was added to the code which occurred once before the main code loop commenced. The calibration worked by sending a digital signal just below the maximum output to the ADC, it was found that setting it to 4000 rather than the full 4095 worked well without sacrificing too much resolution. The output voltage of the ADC was then measured by the microcontroller using its internal power rail which was unaffected. This value was then set as the new maximum voltage and mapped onto the 0-4000 digital range. The circuit diagram for the final circuit is shown below in Figure 3.17.

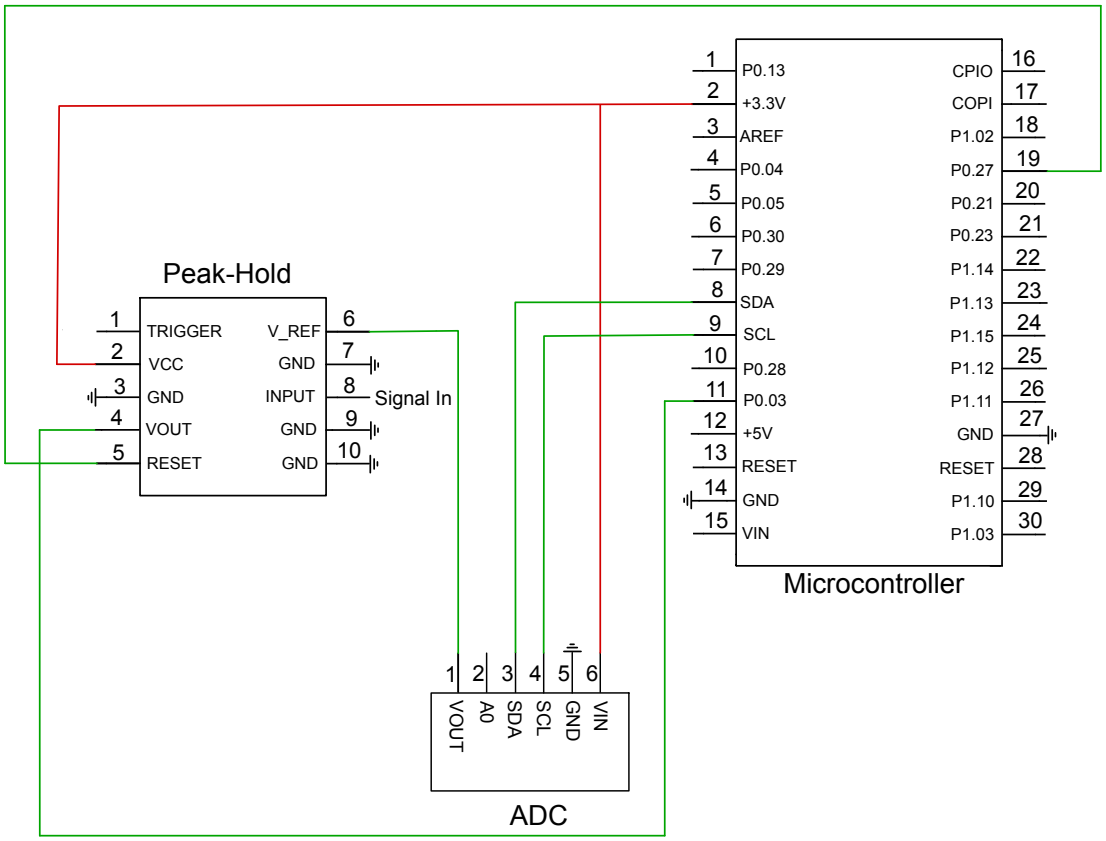

Figure 3.17: Circuit diagram for the detector circuit developed for the project. The red lines indicate a connection to the positive power supply and green lines are data cables both digital and analogue.

3.2.5 Setup and data acquisition

The experimental setup for testing the microcontroller circuit consisted of a pulser connected to a tabletop shaping amplifier which fed into the circuit. For all tests done with this pulser all variables were kept constant and only the output voltage was varied, the settings are shown below in table 3. The shaping amplifier was an Ortec 572A Spectroscopy Amplifier [44] which was required to shape the pulses from the pulser for the peak-hold circuit. Without this the peak-hold circuit could retrigger on the tail of the pulse after resetting. A voltmeter was connected between the amplifier and the circuit

which was used to measure the voltage of the pulses supplied to the circuit with a precision of ±1mV.

Table 3: Pulser settings used for all tests performed for the Arduino microcontroller detector circuit.

Setting	Value
Width	100ns
Rise Time	5μs
Fall time	100ns
Rate	2.5kHz
Delay	250ns

There were two possible methods for acquiring data from the Arduino microcontroller. These were constant data streaming over the USB serial port, or the data could be stored using the Arduino's onboard storage and then retrieved once this was full. The former allowed for live readout of data however this greatly reduced the speed of the microcontroller's code loop. As mentioned in section 3.2.2 this would negatively impact the microcontroller's ability to detect sources with a higher activity. The second method allowed for a much faster code loop as just writing the values to memory is much faster than constantly sending them via the serial port. The drawback of this was that once the memory of the microcontroller was full it would pause for around a second to send all the data. For the testing and prototyping purposes of this project this was considered the best approach. To optimise storage of the data the microcontroller stored the data in histogram form so the number of counts for each channel was recorded not each individual pulse energy. Once the data had been collected it was analysed using the ROOT analysis software.

4 Results

4.1 Canned Scintillator Results

This section presents the data and analysis obtained for the canned scintillator detector developed in this project. The key areas analysed were the SiPM performance, the linearity and resolution of the detector, and add-back analysis is also presented.

4.1.1 Error Evaluation

This section will briefly discuss the determination of the errors in the following sections (4.1.2-4.1.6). For the SiPM testing in 4.1.2 the errors presented correspond to the precision of the instruments that measured these values. Figure 4.2 clearly shows discrete jumps in the values which corresponds to the precision of the bias supply which was used to measure the voltage and current of each SiPM array. The error for the temperature measurement was also determined in this way. As discussed in section 3.1.5 for the sections that evaluated the performance of the detector's resolution and linearity, a Gaussian function with a linear background was used. Figure 4.1 shows this function fitted to a 661.7KeV peak from a ^{137}Cs source.

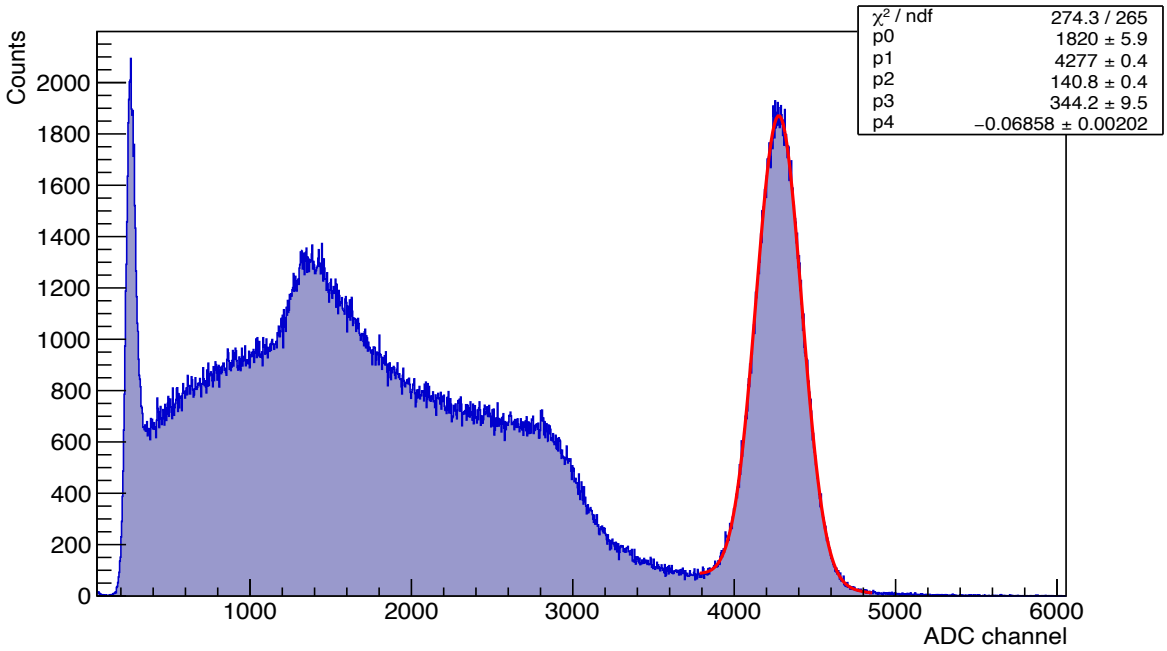

Figure 4.1: Example of an energy spectra gathered from a ^{137}Cs source with a Gaussian plus linear background function (shown in red) fitted to the 661.7KeV peak. The parameters shown in the top right information pane correspond to Eq. 3.1 in the following way: P0 to $\boldsymbol{a}$, P1 to $\boldsymbol{\mu}$, P2 to $\boldsymbol{\sigma}$, P3 to $\boldsymbol{c}$ and P4 to $\boldsymbol{b}$.

As can be seen from the information panel in the top right of Figure 4.1 the errors produced for the Gaussian fit were very optimistic. These errors were too low to be considered reasonable considering the histogram had been binned to 4 channels per bin. To determine errors that would be more suitable to represent the uncertainty of the measurement a manual approach was taken. This involved the manual inspection of the energy spectrum shown in Figure 4.1. Due to variations in the bin heights of the histogram the average height of the peak over 12 bins was taken. The error for this measurement was taken as the standard error of the 12 heights, given by $SE = \frac{\sigma}{\sqrt{n}}$. The error in the centroid value was taken to be half the range over which the height was measured, 6 bins containing 24 channels. The full height was then used to measure the FWHM, the error for which was found by using the error in the height to find the maximum and minimum

half heights. The error added by the binning was also factored into this. Table 4 below shows the errors determined for each parameter.

Table 4: The Gaussian parameters and FWHM of a 661.7KeV peak from a ^{137}Cs energy spectra gathered by Crystal 1. The values and their uncertainties were determined by manually inspecting the peak.

Parameter	Value
Height ($\boldsymbol{a}$)	1820±10
Centroid (μ)	4280±20 ch
Sigma (σ)	140±2 ch
FWHM	330±6 ch

The errors generated using this method appeared to better capture the uncertainty in the measurement that those generated by the ROOT analysis. For this reason, the percentage error in these measurements in Crystal 1 were used as the errors in the parameter values found by ROOT for the other crystals. This was repeated for the Add-back analysis in section 4.1.6 and the seal longevity testing in section 4.1.5.

4.1.2 SiPM testing

The first tests done on the detector were the testing of the 2x2 Hamamatsu SiPM arrays attached to each NaI(Tl) crystal. The arrays were tested while the detector was exposed to a ^{137}Cs source and the current and voltage could be observed from the bias supply. Figure 4.2 shows the voltage and current over a 5-minute period for the SiPM array attached to Crystal 1 in the detector. The values from this test for each of the arrays is shown in Table 5.

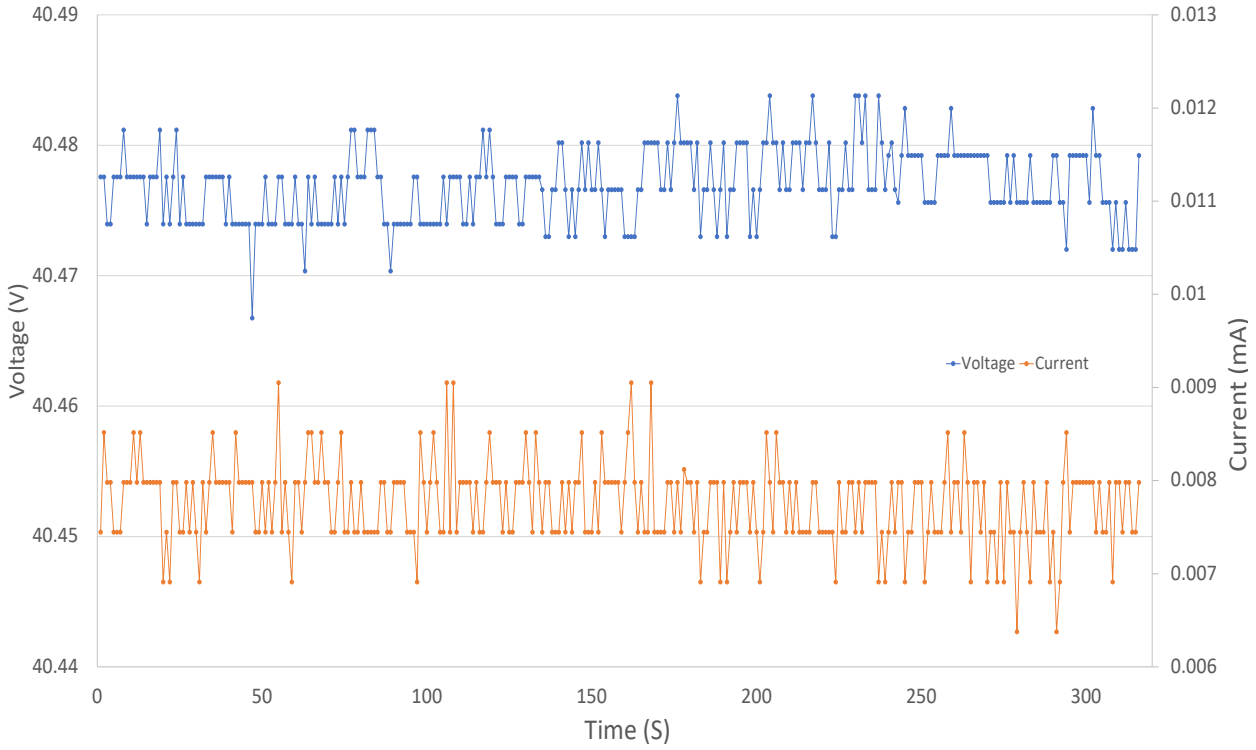

Figure 4.2: Voltage and current for the SiPM array on Crystal 1 over a 5-minute period. The blue line shows the voltage, and the orange line shows the current, with the voltage axis shown on the left and the current axis on the right.

Table 5: Table of voltage and current mean values over a 5-minute sample while the detector was exposed to a ^{137}Cs source.

SiPM	Voltage (V)	Current (mA)
1	40.477±0.004	0.0078±0.0005
2	40.476±0.004	0.0070±0.0005
3	40.480±0.004	0.0086±0.0005
4	40.482±0.004	0.0084±0.0005

The temperature variation was also measured during this test. Over the short test the temperature stayed at an average of 23.18±0.01°C, this was expected due to the short time and large thermal mass the SiPMs were in contact with.

4.1.3 Calibration and Linearity Testing

The detector required an energy calibration due to the non-linear nature of NaI(Tl) and SiPMs. To do this calibration an ^{152}Eu and a ^{137}Cs source were used to generate a spectrum with the detector, the spectrums for these sources together are shown in Figure 4.4. Known energy peaks from these sources were then identified on the resultant spectra. The ADC channel number of each of these peaks was then compared to their known value. The ^{152}Eu source was used due to its large number and large distribution and easily identifiable energy peaks. The ^{137}Cs was used due to its very strong 661.7KeV peak which does not overlap a major peak of the ^{152}Eu and thus would act as an easily identifiable reference peak. For each crystal the following energy peaks were used for the calibration: 41KeV, 121KeV, 244.7KeV, 344.3KeV, 661.7KeV, 778.9KeV, 1112.9KeV, 1408KeV. The only exceptions were the omission of the 1408KeV peak for Crystal 2 and the 1112.9KeV peak for Crystal 4, instead of which the 964keV peak was used, this was due to the low number of counts in these peaks.

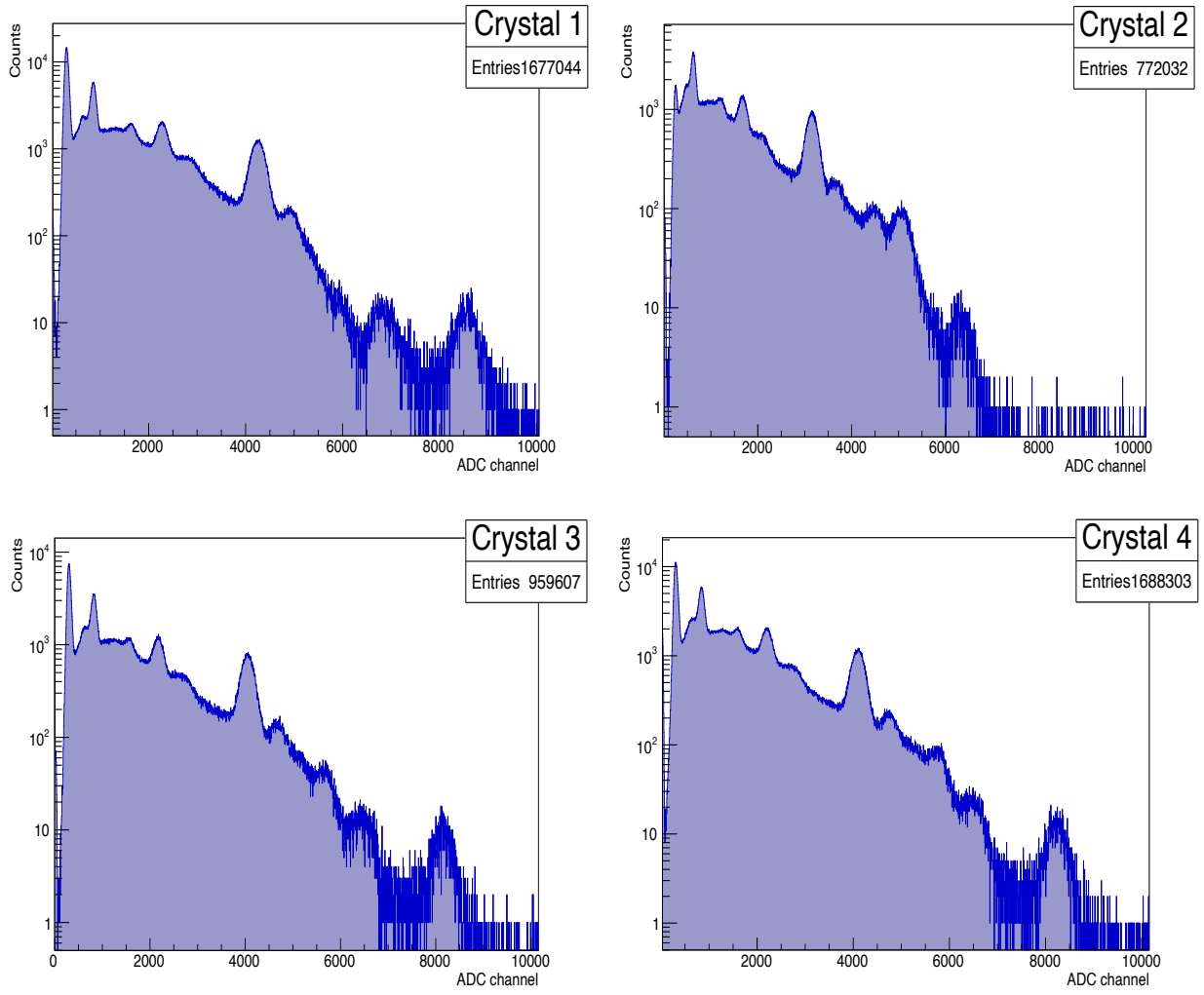

Figure 4.4: Energy spectra gathered from ^{152}Eu and ^{137}Cs sources spectrum for all 4 crystals. The centroids for the major peaks in these spectrums were taken and compared to their know values to generate a calibration function.

The centroids found using the Gaussian fit were then plotted against their known energy value. This plot was then fitted with a second order polynomial function to find the energy calibration function. Figure 4.5 shows these plots and the calibration function associated for each crystal.

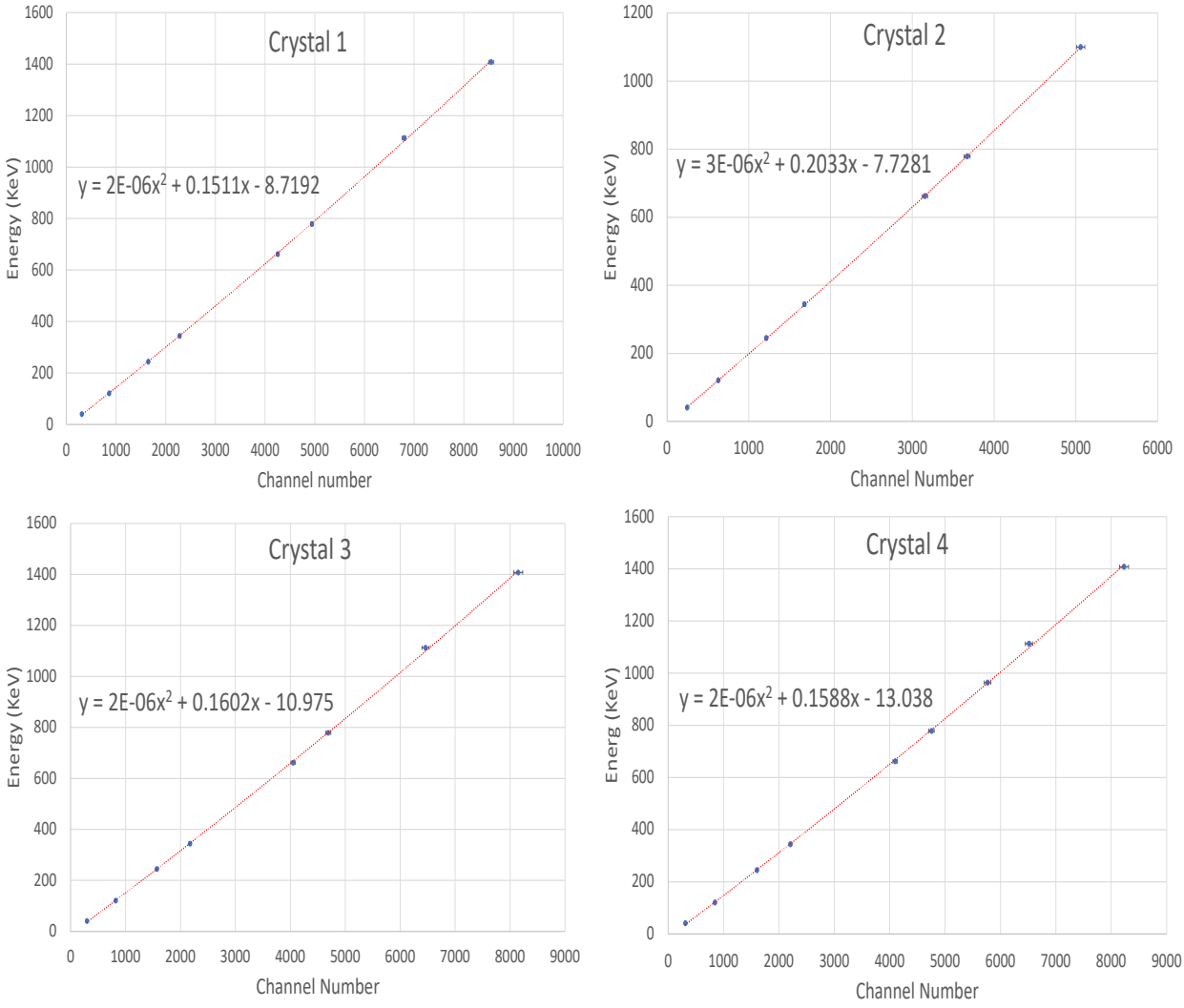

Figure 4.5: Plot of channel number of energy peaks plotted against their known energy values. Each plot has been fitted with a second order polynomial (dotted line) to give a calibration function for each detector which is shown by the equation next to each plot.

A second order polynomial was fit to the data in Figure 4.4 to produce a calibration function accounting for nonlinearity. This fit was done factoring in the uncertainty in the measured channel number from Figure 4.2. The percentage deviation of the measured channel response from the second order polynomial is shown below in Figure 4.6.

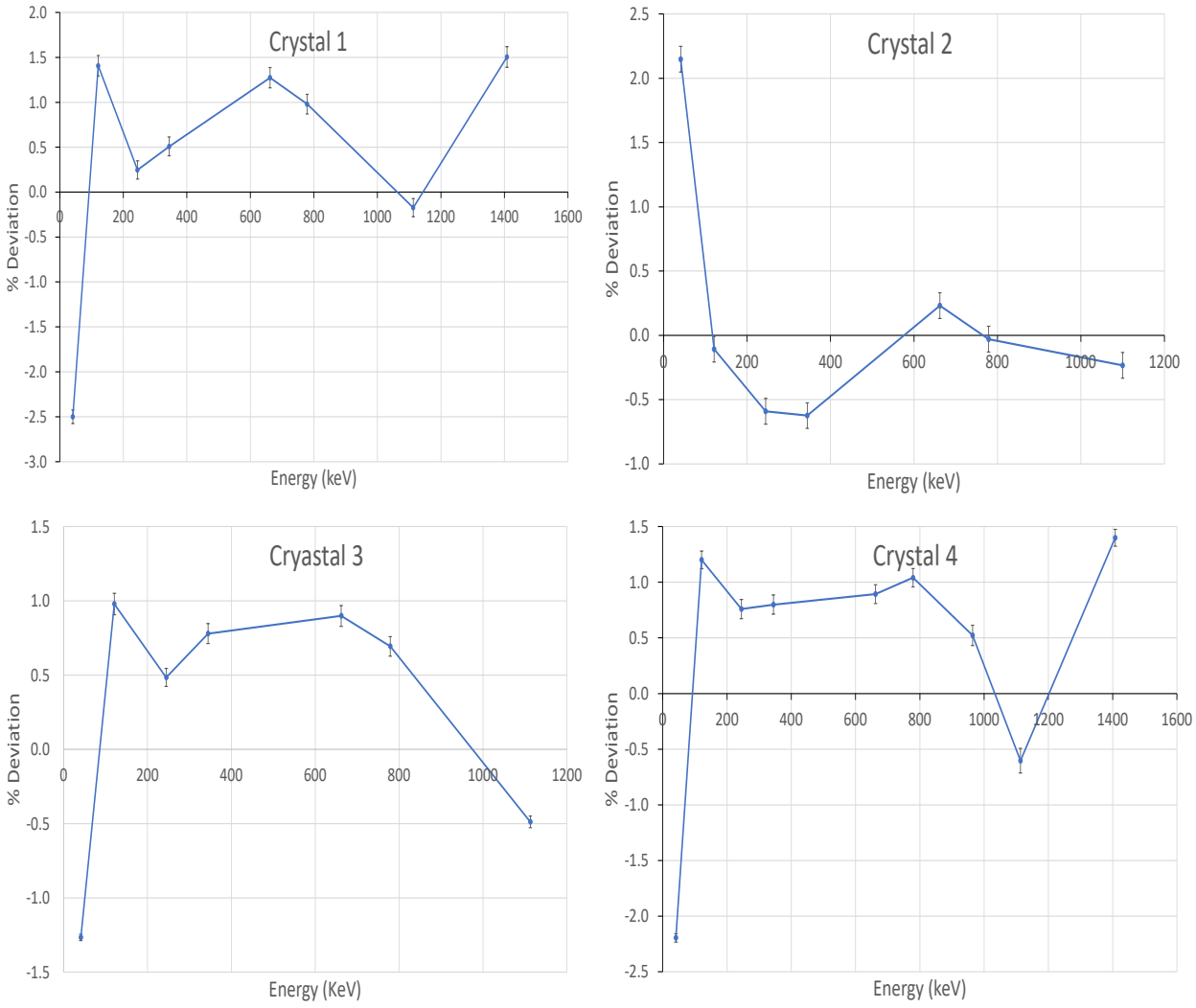

Figure 4.6: Percentage deviation of the measured peak positions from a ^{152}Eu and ^{137}Cs source spectrum from the predicted response produced by the second order polynomial from Figure 4.5. The blue line is to guide the eye only.

4.2.4 Resolution Testing

The resolution of Crystal 1 was tested using a ^{137}Cs source. Crystal 2 was used due to it having a single easily identifiable γ ray peak at 661.7KeV. The peak was fitted using the same gaussian and linear background fit that was used in section 4.1.2, these plots are shown in Figure 4.13 below. Table 6 shows the resolutions of each crystal for the 661.7KeV energy peak measured from this data. The energy calibration function determined for each crystal in section 4.1.2 was then used on the data to obtain the calibrated energy resolution of for each detector crystal. This is shown in table 7.

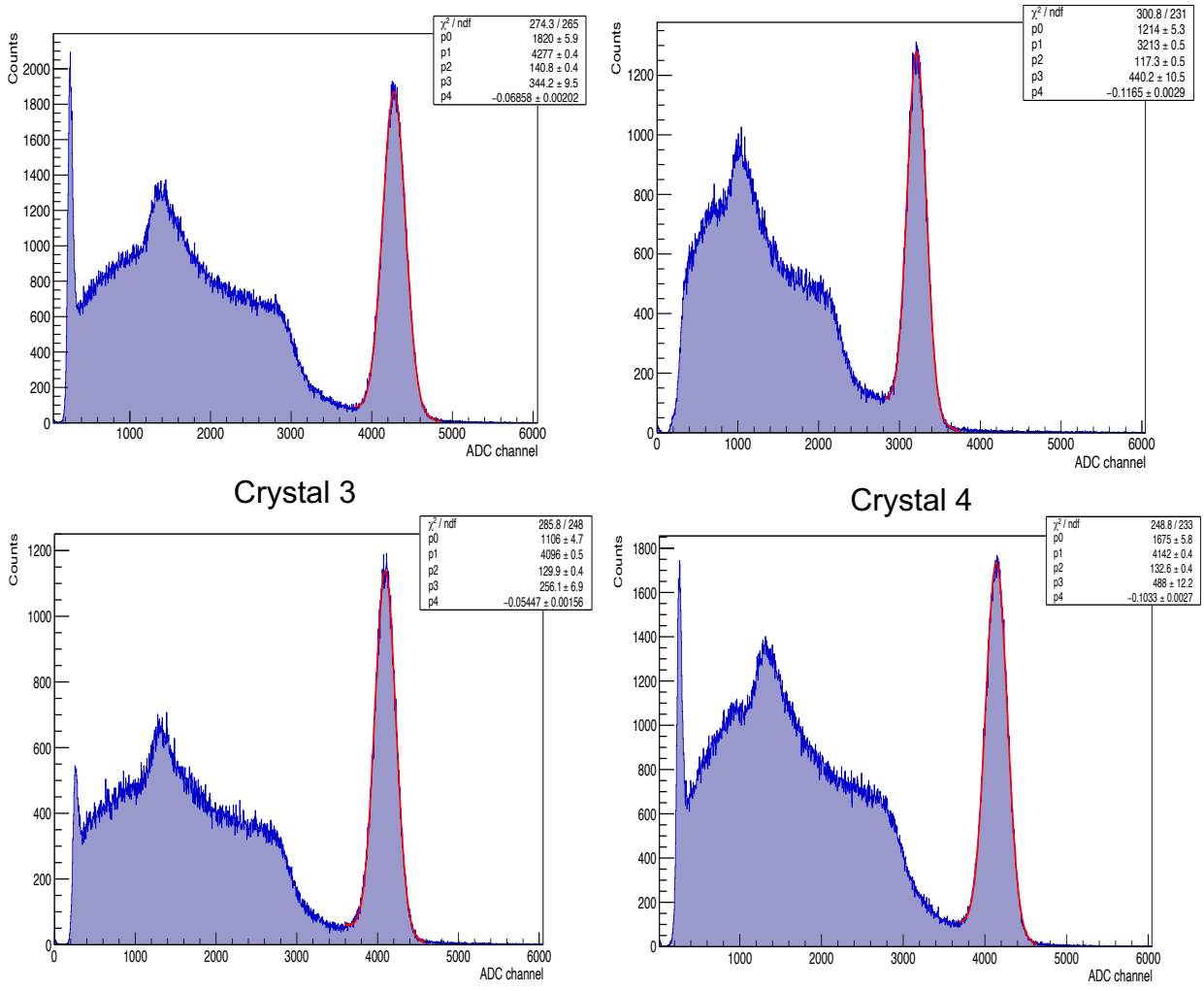

Figure 4.6: Plot of the ^{137}Cs energy spectrum for each crystal with Gaussian plus linear background fitted (shown in red) on the 661.7KeV peak.

Table 6: Non-linearity-corrected raw resolution for the 661.7KeV energy peak of a ^{137}Cs source for each crystal in the detector.

Crystal	Mean (Ch)	FWHM (Ch)	Resolution (%)
1	4280±20	332±6	7.8±0.1
2	3210±20	276±5	8.6±0.2
3	4090±20	304±6	7.4±0.1
4	4140±20	311±6	7.5±0.1

Table 7: Linearity-corrected energy resolution for the 661.7KeV energy peak of a ^{137}Cs source for each crystal in the detector.

Crystal	Mean (KeV)	FWHM (KeV)	Resolution (%)
1	674±4	56±1	8.3±0.2
2	676±4	61±1	9.1±0.2
3	678±3	54±1	7.9±0.2
4	664±3	52±1	7.8±0.2

4.2.5 Hermetic Seal Testing

One of the most important aspects of the detector design and therefore of this project was the effectiveness and longevity of the hermetic seal. To test the performance of the seal a set of data was taken two months after its initial assembly. Ideally this test would be done over a longer period, but this was the longest possible for this project. The data

shown in Figure 4.7 was gathered using ^{137}Cs source as used in the previous sections. The resolutions gathered from these tests are shown in table 8.

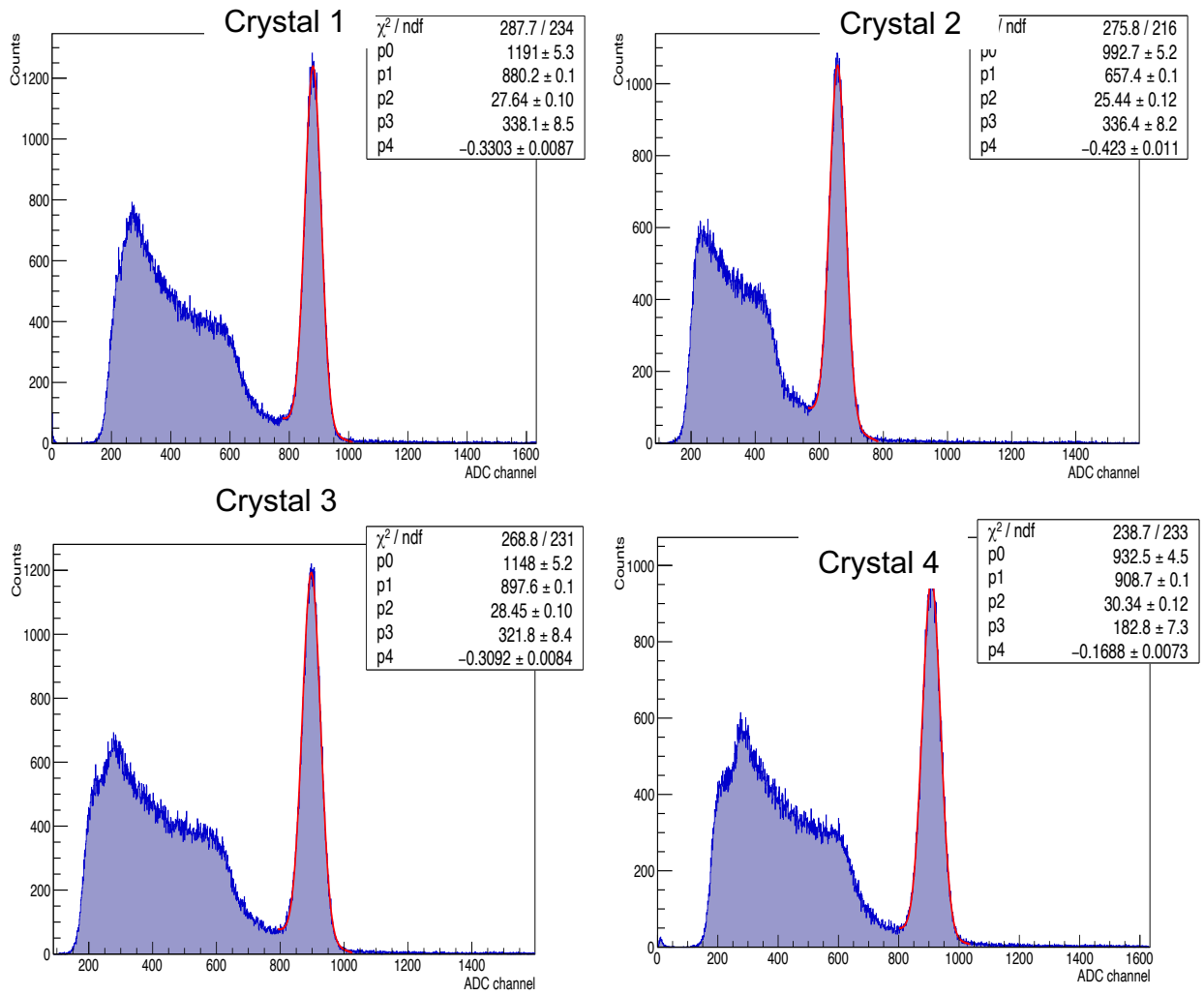

Figure 4.7: Plot of a ^{137}Cs spectrum for each crystal in the detector 2 months after being hermetically sealed. A Gaussian plus linear background function (shown in red) has been fitted to the 661.7KeV peak.

Table 8: Non-linearity-corrected raw resolution obtained for the 661.7KeV peak of a ^{137}Cs source, two months after hermetically sealing the detector and placing in atmosphere.

Crystal	Mean (ch)	FWHM (ch)	Resolution (%)
1	910±20	71±3	7.9±0.4%
2	657±10	60±3	9.1±0.4%
3	880±20	66±3	7.5±0.3%
4	900±20	76±3	7.5±0.3%

4.2.6 Add-Back

As discussed in section 2.2 and 2.3 sometimes only part of the energy of an incident γ ray is absorbed into the scintillator and the rest of the energy can be lost in the form of a scattered photon leaving the detector. In the case of a cluster detector, like the one developed in this project, these scattered photons can often scatter into one of the other crystals in the detector. In normal independent operation each crystal could detect some of these photons and they would contribute to the Compton background. However, if all events are measured with good time resolution, these scattering events across crystals can be grouped as coincidences (events that are captured within a coincidence time window). This is possible because the time difference between these events is very small as γ rays travel at the speed of light. The process of grouping events across crystals and adding their energies is known as add-back.

To test the add-back performance of the detector, data taken using a ^{152}Eu and a ^{137}Cs source was grouped into coincidences with a 100ns window. These coincidences between each pair of crystals are shown below in Figure 4.8. The data shows no coincidences between Crystal 2 and Crystal 3 which was due to a DAQ issue. When this was discovered the time restrictions of the project meant no more data could be

gathered. These coincidences were then be summed together to find the full energy deposited by the γ ray. This data is shown in Figure 4.9 where the energy calibration calculated in section 4.2.2 is applied and the resolutions are shown in table 9.

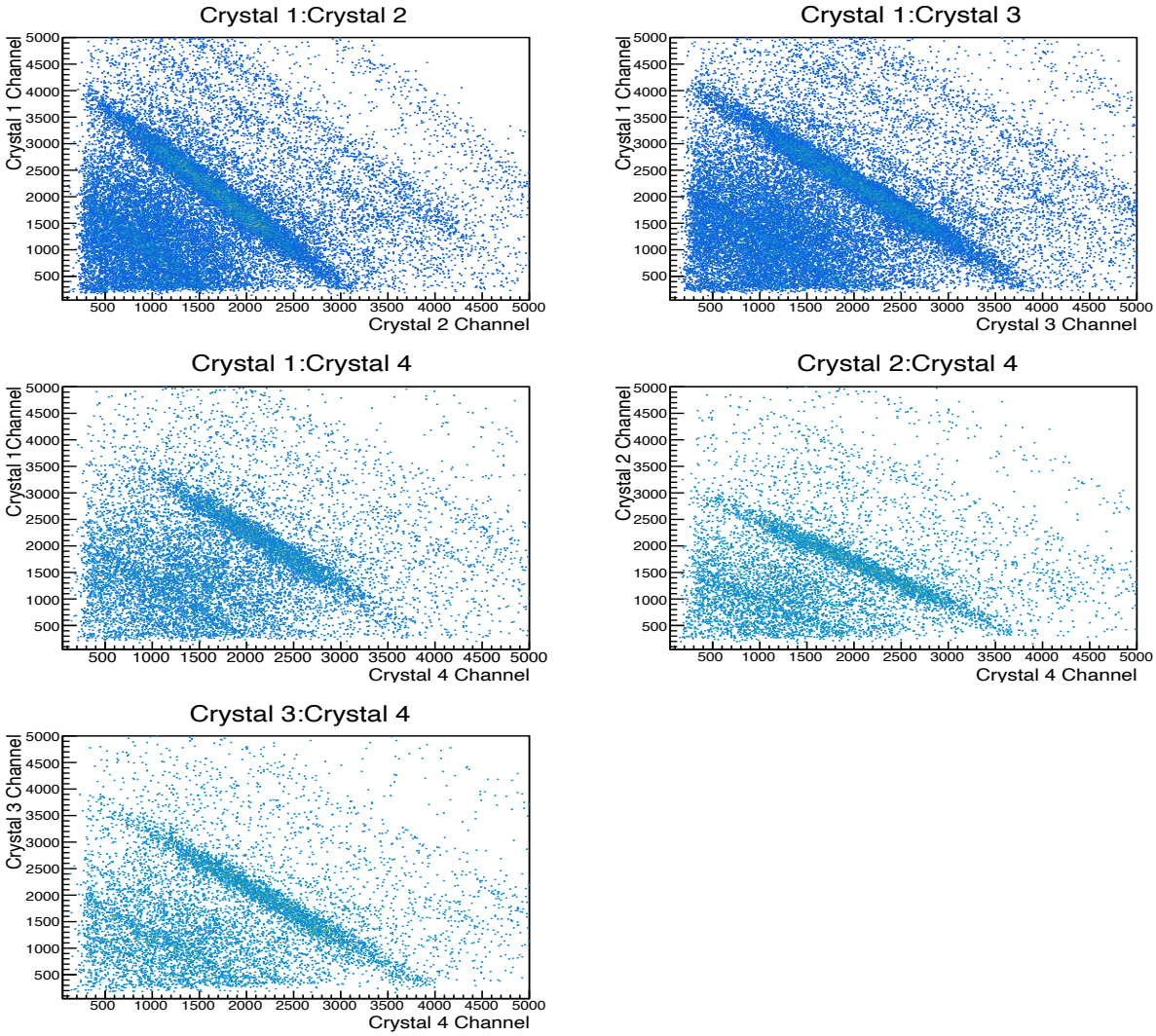

Figure 4.8: Coincidence plot of the energy measured by one crystal versus the energy measured by another crystal of the module for ^{152}Eu and a ^{137}Cs sources with a coincidence window of 100ns. Density of plotted events is represented by colour, low density shown in light blue with higher density shown in green. The 661.7KeV peak of the ^{137}Cs source can be seen by the highest density diagonal strip.

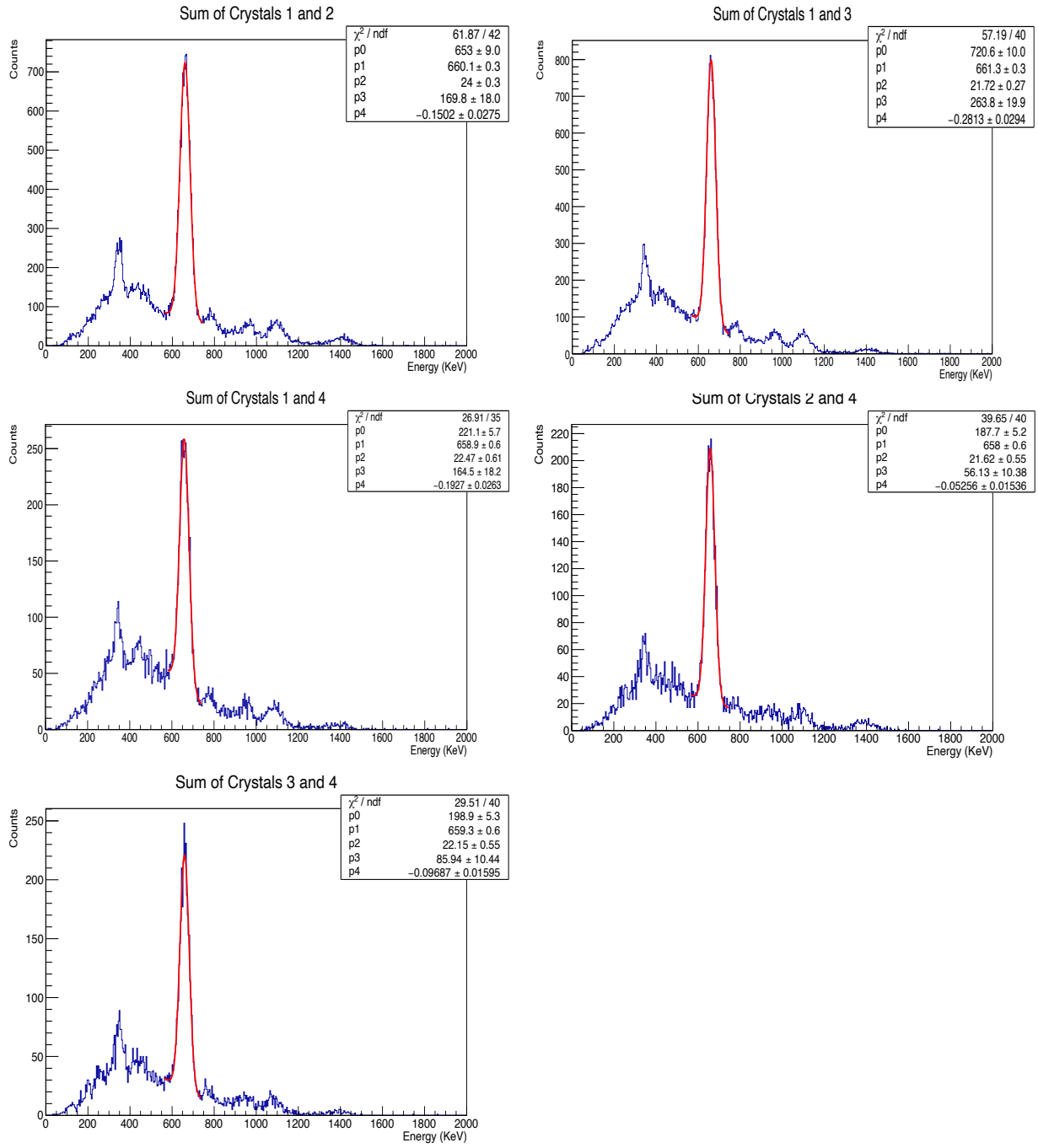

Figure 4.9: Plot of the summed energy of coincidence events between each pairing of crystals for ^{152}Eu and ^{137}Cs sources within a 100ns time coincidence window. A Gaussian plus linear background fit has been applied (shown in red) to the 661.7KeV peak.

Table 9: Resolutions of each crystal pair using the add-back method. Using the detector in add-back mode greatly enhanced the resolution as was shown in section 4.2.5.

Crystal pair	Mean (KeV)	FWHM	Resolution
1 and 2	660±10	57±4	8.6±0.9%
1 and 3	660±10	51±3	7.7±0.8%
1 and 4	660±10	53±4	8.0±0.8%
2 and 4	660±10	51±4	7.7±0.7%
3 and 4	660±10	52±4	7.9±0.8%

The time differences between events that were inside the coincidence window and thus were counted as coincidences are shown for each crystal in Figure 4.10.

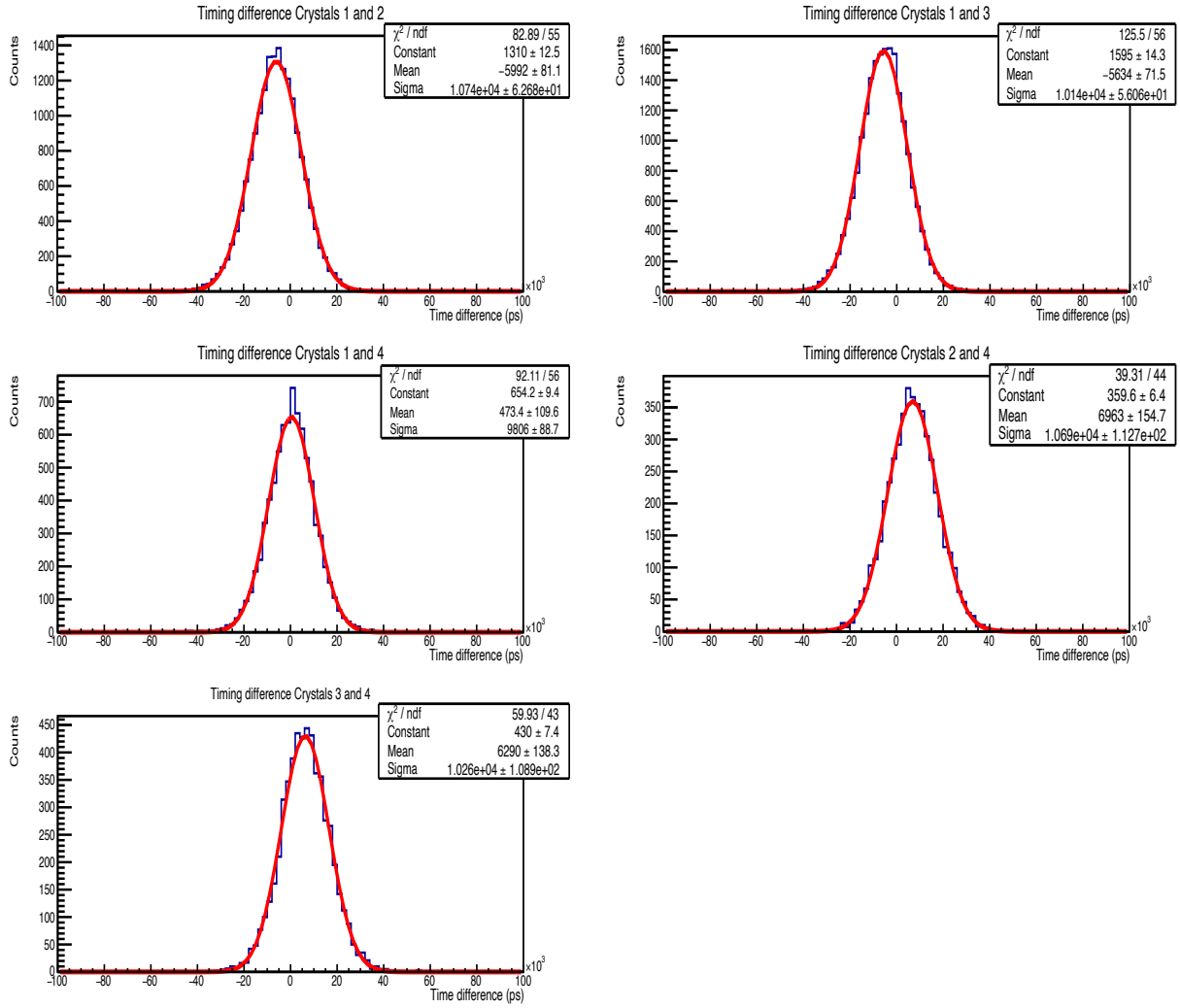

Figure 4.10: Plot of the timing difference between events in coincidence for a 100ns coincidence window using an ^{152}Eu and a ^{137}Cs source.

4.2 Microcontroller circuit

The results for the testing of the microcontroller integrated circuit are presented below. The minimum voltage threshold was tested along with the inherent linearity and resolution of the circuit. The noise and its effect on resolution is also reported on.

4.2.1 Analysis and Error Evaluation

This section will discuss the determination of the errors in the following sections (4.2.2-4.2.4). Similarly to the detector analysis, the ROOT analysis software was initially used to fit a Gaussian function to the peaks produced by pulser input to the detector circuit, Figure 4.11 is an example of this.

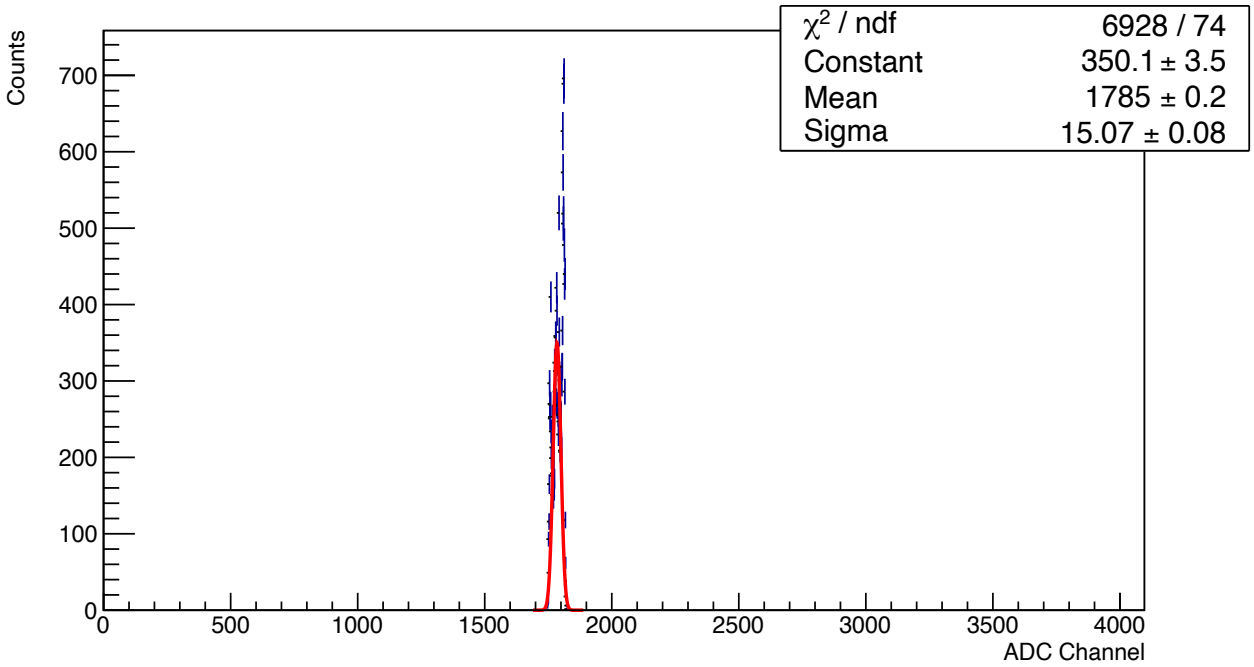

Figure 4.11: Histogram of 1.5V input from a pulser to the microcontroller circuit with 40mV threshold. The histogram is fitted with a Gaussian function (red curve) to find the peak, mean and sigma value.

As can be seen from Figure 4.11 the gaussian fit did not describe the height of the peak well, this was due to the data being slightly skewed. Instead of fitting a Gaussian function to determine the centroid and the spread of the peak, the mean, μ, and the standard deviation σ were calculated individually to quantify these. The standard deviation is given by Eq. 4.1. The ROOT analysis software was used to calculate these values and their statistical errors. The error in the mean was calculated by ROOT using the standard error, which was discussed in section 4.1.1 and the error in the standard deviation was found by taking the standard deviation in the estimate of the standard deviation. For the 1.5V input peak that was shown in Figure 4.11 this method gave a mean of 1789.7±0.1 and a standard deviation of 19.0±0.1.

$$\sigma = \sum_{n=1}^{n} (x_i - \mu)^2 \qquad (4.1)$$

4.2.1 Threshold Testing

The microcontroller's voltage threshold was the first aspect tested. To test this a pulser was used to input a known voltage signal to the microcontroller circuit. This was done over a range of threshold voltages. The pulser signal was kept at a consistent voltage of 1.5V for each threshold test. The lowest threshold voltage without a significant low voltage noise was 38mV. Below this threshold a low voltage peak would occur due to noise. In Figure 4.12 where a threshold voltage of 37mV was set this low voltage peak is clearly visible.

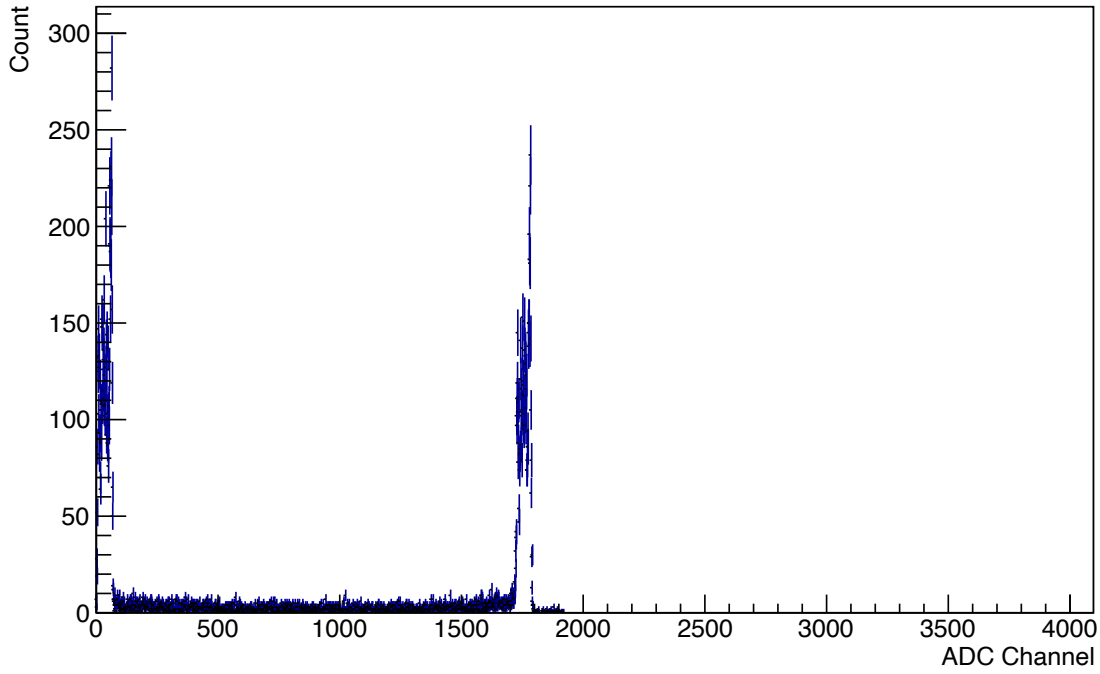

Figure 4.12: Plot showing a 1.5V input from a pulser to the microcontroller circuit with 37mV threshold. A large amount of noise in the lower ADC channels can be seen due to the threshold being set too low.

4.2.2 Shaping Time Testing

The pulses input to the Microcontroller were done so via a shaping amplifier. A test was done to determine optimal shaping time for the setup. This was done by varying the shaping time of the amplifier while maintaining all other variables. For this test the input pulses had a voltage of 1.5V. Figure 4.13 shows the FWHM for the 1.5V peak at each shaping time.

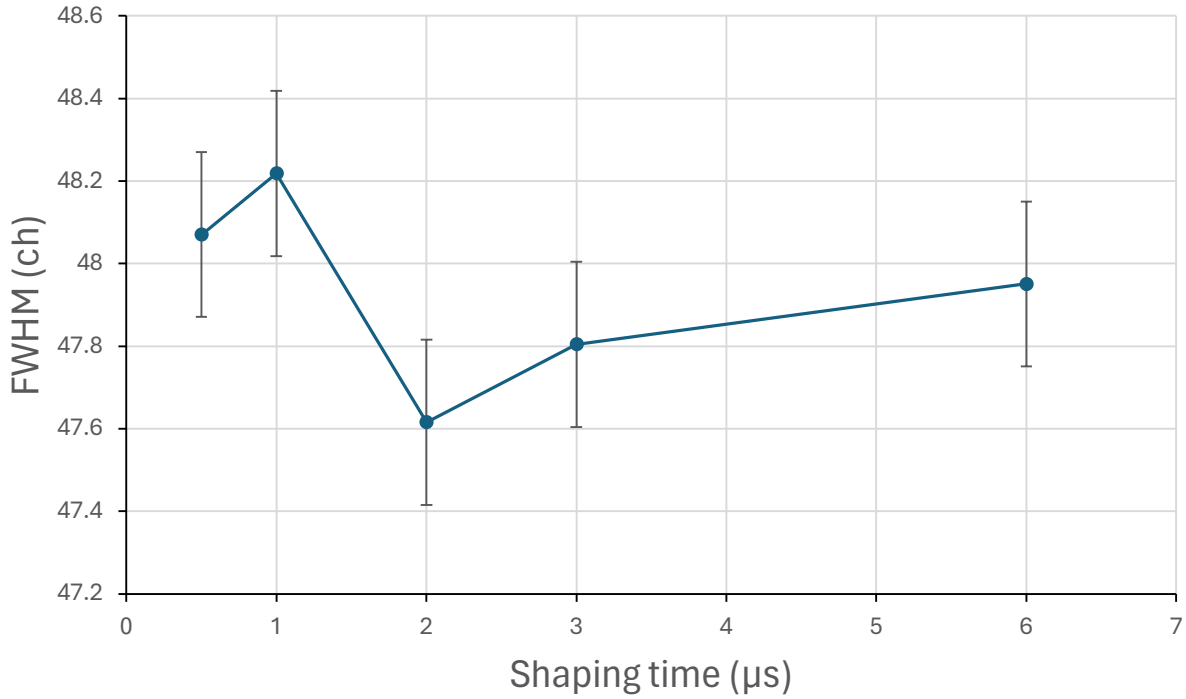

Figure 4.13: Plot of the FWHM against shaping time for a 1.5V input peak to the microcontroller detector circuit. A dip in the FWHM can be seen for a shaping time of 2µs however this overlaps in error with both 3µs and 6µs. The blue curve is to guide the eye only.

A shaping time of 10µs was also tried but this was too long and caused the peak-hold circuit to trigger on the tail of pulses. Figure 4.13 show that 2µs, 3µs and 5µs shaping times overlap in error however, 2µs was chosen as the shaping time for the subsequent tests. This was due to it having the lowest maximum FWHM within error of the three times.

4.2.3 Linearity Testing

The linearity of the microcontroller was determined by measuring the mean ADC channel number for known voltage peaks across the microcontroller's operating voltage range. This was done from 40mV up to 3.2V in 10mV intervals.

Figure 4.14 below shows each ADC channel centroid plotted against the input voltage from the pulser. The Figure shows that the microcontroller followed a linear response until after 2.9V where it started to become more nonlinear. It was decided to exclude these points in the subsequent analysis as they were deemed to exhibit a much more nonlinear response than that of the rest of the voltage range.

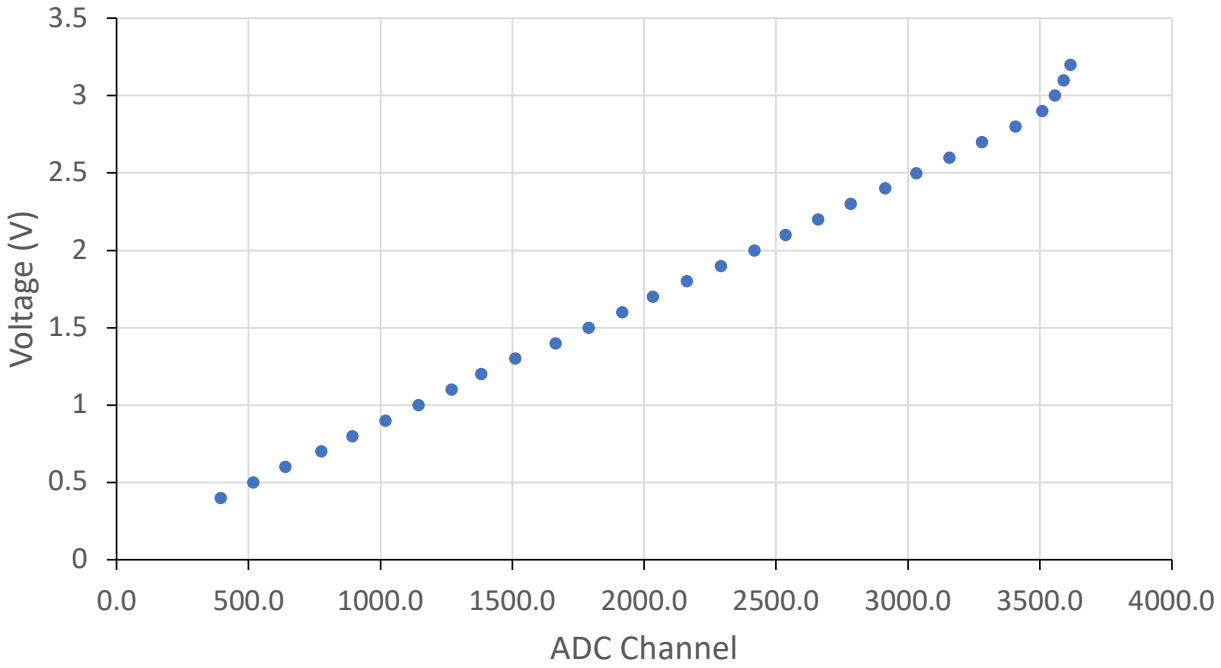

Figure 4.14: ADC channel against the input voltage for the microcontroller circuit. Each voltage was measured with a 40mV threshold.

A linear function of the form $y = ax + b$, was fitted onto the data to give the idealised linear response, this is shown in Figure 4.15. This was possible as in theory the ADC inside the microcontroller should have a linear response.

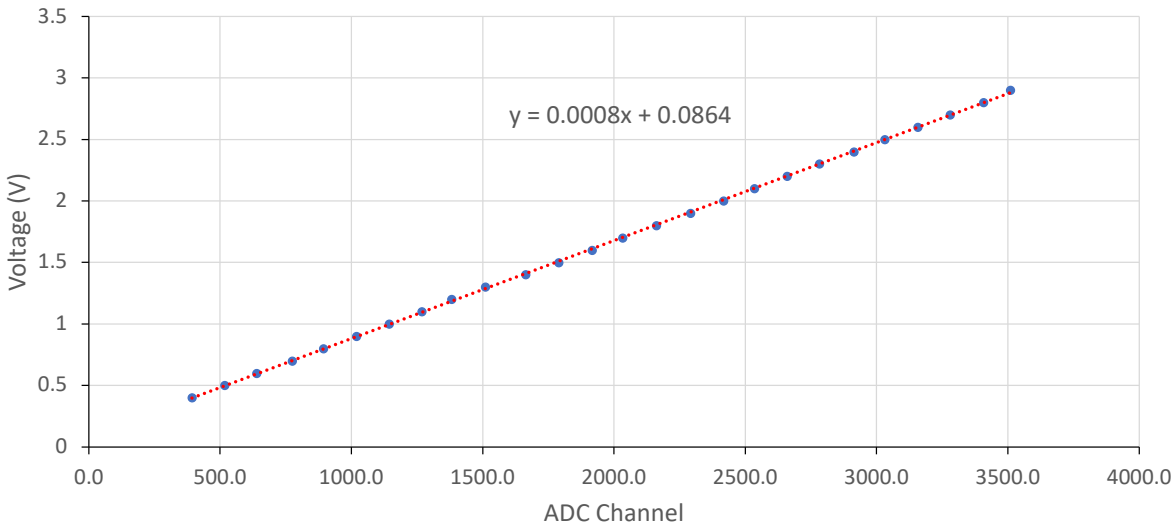

Figure 4.15: Voltage to ADC channel plot in the range of 40mV to 2.9V**.** A linear fit has been added (red dotted line) to show the ideal linear response function. The plot includes error bars however, these are not visible on this scale.

The ideal linear function was then used to determine the percentage difference of the measured point to the ideal line. This is shown in Figure 4.16 and gives a measure of the nonlinearity.

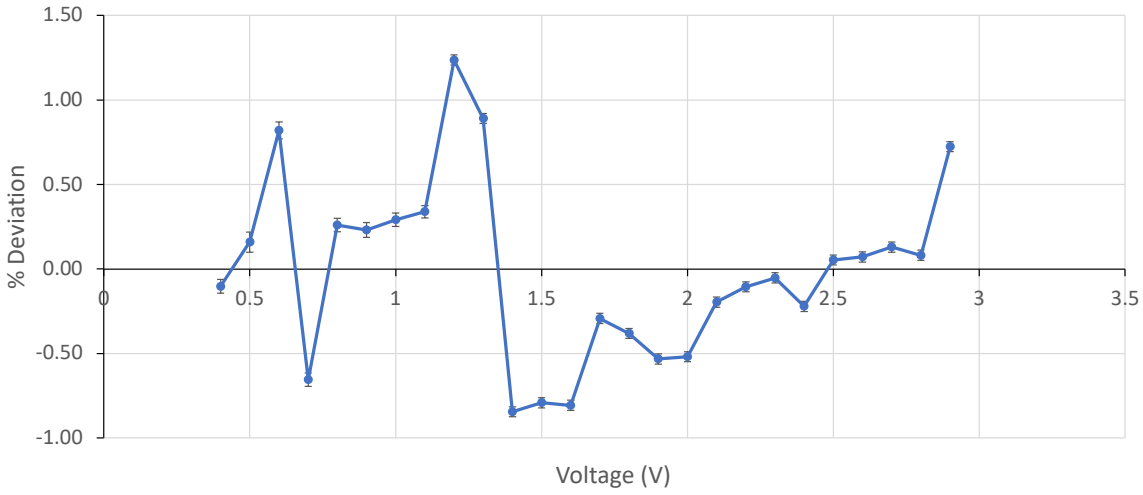

Figure 4.16: Percentage deviation of the measured response from the ideal linear response of the ADC against the input voltage. The blue curve is to guide the eye only.

4.1.3 Noise and Resolution testing

The same data collected for the calibration and linearity testing in section 4.2.2 was used to test the noise levels and the instrument resolution of the microcontroller circuit across its operating range. The average FWHM across this range was calculated to be 44.5±0.2 channels. Figure 4.17 shows the FWHM for inputs over the operating range of the microcontroller.

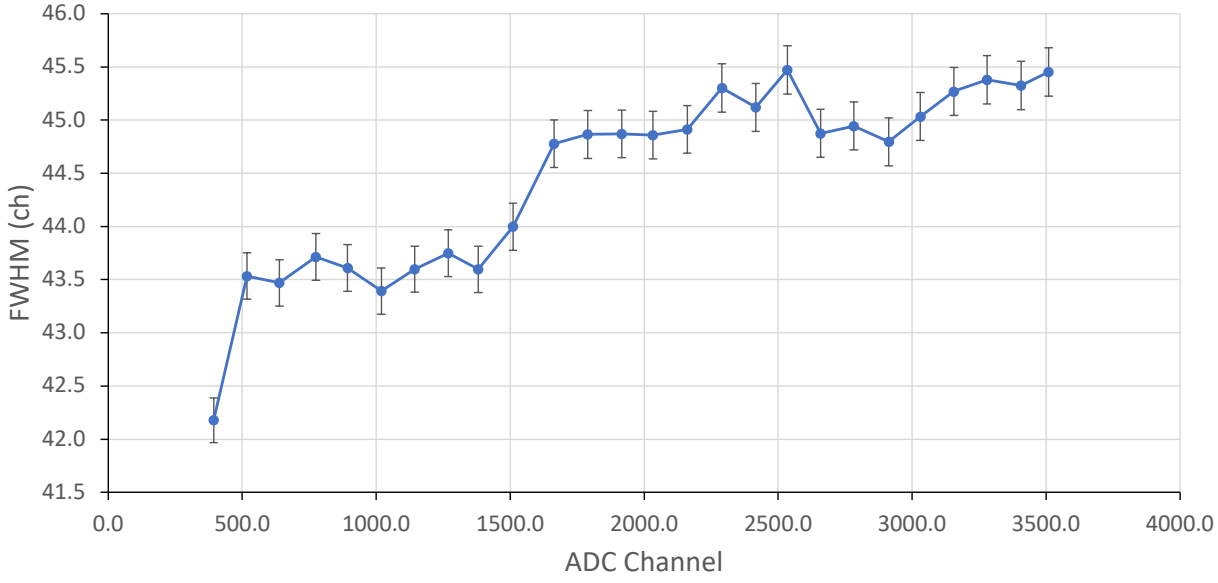

Figure 4.17: Microcontroller ADC channel resolution plotted against ADC channel. This is for the input interval of 0.4V to 2.9V input by a pulser. The blue curve is to guide the eye only.

5 Discussion of Results and Future Outlook

5.1 Discussion of results

This section discusses the outcomes and data presented for the canned scintillator detector and microcontroller integrated circuit in section 4. The data is evaluated and compared to other experimental work. Potential future steps for the work carried out is also presented. This includes a new design for the aluminium housing, utilising a clamping mechanism derived from the one tested in this project.

5.1.1 SiPM Performance

The SiPM arrays used in this experiment were 2x2 arrays made up of 6mmx6mm s14160-6050HS [35] SiPM modules which at the time of writing this thesis constitutes the latest SiPM photosensor from Hamamatsu. These SiPMs are individually rated for a maximum dark current of 7μA [35]. The arrays, consisting of four of these individual SiPMs, therefore have a maximum dark current of around 28μA.

Table 5 shows the average current for the four arrays used in this work when exposed to γ radiation of low intensity, all arrays operated well below the maximum. These averages include signal pulses caused by incident photons being detected meaning that the dark current was below the numbers shown in table 5. However, the performance of the SiPMs is greatly affected by temperature. These tests were done at around 23°C as shown in section 4.1.2, this is lower than the temperature at which the SiPM dark currents are stated for by the manufacturer.

The SiPMs used in this project had a temperature coefficient of the recommended reverse voltage, $\Delta T V_{op}$, of 34mV/°C [35], here ΔT is the change in temperature and V_{op} is the operating voltage. This was used to calculate a systematic error in the gain of the array. The temperature was shown to be measured with a precision of $\pm$0.1°C which when

multiplied by the temperature coefficient gave an error of ±3mV in the overvoltage. Figure 3.13 shows the relationship between the overvoltage and the gain. As this is a linear relationship, the gradient of this line could be used to estimate an error in the gain. This gave an error in the gain of ±0.04%. Hence, for a typical pulse the variation in the gain uncertainty is negligible compared to other factors affective the resolution as long as the temperature is monitored with 0.1°C precision and the voltage is compensated.

5.1.2 Detector Resolution

NaI(Tl) crystals have been extensively tested making them easily benchmarked and compared. An experiment in 2017 used a 2-inch diameter x 2-inch (50.8x50.8mm) cylindrical block of NaI(Tl) as a scintillator with a 4x4 (24x24mm) array of SensL MicroFC 60035 SiPMs. This serves as an excellent point of reference for the detector developed in this project. The detector in that project achieved a resolution of 8.1±0.1% after calibration for a 661.7KeV peak. The experiment also reported on the detectors performance with a larger 6x6 SiPM array (36x36mm). With the larger array the detector was measured as having a resolution of 7.6±0.3%. [45]

The detector developed in the project presented in this thesis performed comparably to the cylindrical detector when the cylindrical detector was using a 4x4 SiPM array. As Table 6 shows Crystal 1 performed slightly worse than the cylindrical detector, Crystals 3 and 4 both outperformed it and Crystal 2 was significantly worse. When compared to the cylindrical detector with the larger 6x6 array Crystals 3 and 4 both overlap within errors with that detector. This result is expected as the larger array of the cylindrical detector will produce a better resolution.

Crystal 2 performed much worse than the other detector which was to be expected due to the damage sustained to it during wrapping, as shown in Figure 3.2. The damage sustained to Crystal 4 however appears to have had no observable impact on the

performance as this was the crystal with the best resolution. Figure 5.1 shows the comparison of the ^{137}Cs and ^{152}Eu spectrums for Crystal 1 and Crystal 2.

As the above Figure 5.1 shows, the crack in Crystal 2 has had a dramatic effect on the crystal's performance. The energy of each peak has been shifted down; this indicates that less light was collected as the rest of the parameters are kept similar between the two crystals. This is likely due to the cracks in the crystal creating boundaries within the crystal which causes photons to scatter out of the crystal or become trapped between the two pieces of crystal. Given that the four NaI(Tl) crystals had originally very similar performance, by comparing the peak positions from these two crystals a light-loss factor

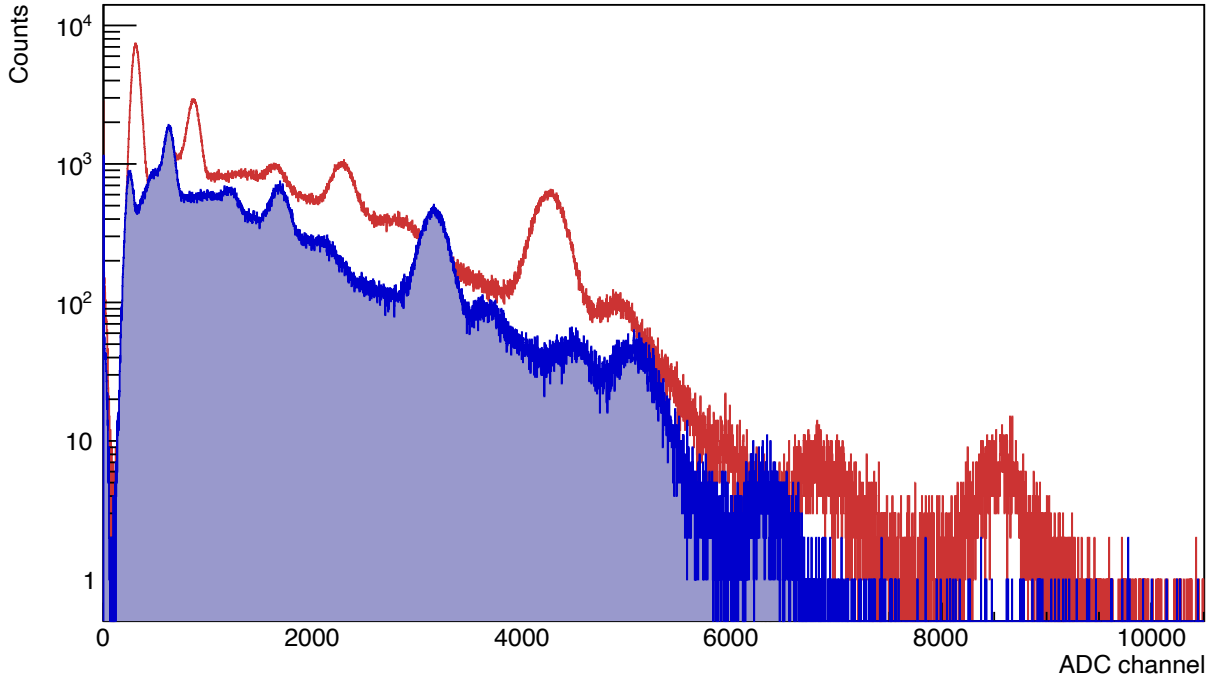

of around 75% was determined.

Figure 5.1: Plot showing the spectrum for ^{137}Cs and ^{152}Eu sources gathered by Crystal 1 (red) and 2 (blue). The peaks for Crystal 2 have much lower channel numbers and therefore energy compared to Crystal 1.

5.1.4 Add-Back Performance

The add-back data presented can be used to determine if there was optical crosstalk between pairs of crystals. Figure 4.8, which shows the channel number of coincidence events for pairs of crystals plotted against one another, shows the events forming clear diagonal bands. This diagonal correlation is due to Compton scattering between crystals where a photon has deposited some of its energy to one crystal and the rest of it in the other. This gives rise to the $x + y = E$ lines that are observed. The most prominent of these lines is due to the 661.7KeV γ rays from the ^{137}Cs source with other lines being formed by peaks from the ^{152}Eu source. If there were optical crosstalk present, then other correlations would be observable other than the Compton scatter correlation. From this it can be determined that there was no observable crosstalk between crystals.

The crystals combinations that appeared to have the most events were Crystals 1 and 2, and 1 and 3. This is unsurprising as these pairs are directly adjacent to each other and a scattered photon from one crystal is more likely to be absorbed by a neighbouring crystal. The pairing of 1 and 4 also follow this expectation, having fewer events when summed than the previously mentioned pairings due to being diagonal from one another. When looking at the pairings of 2 and 4, and 3 and 4, this trend does not continue. These pairs are directly adjacent so would be expected to have similar number of events to the other adjacent pairs. Crystal 4 in all pairings had very few counts. This could be due to the positioning of the source although this was always placed facing the end opposite to the connector end of the detector to try to ensure each crystal was exposed to equal intensity.

5.1.5 Hermetic Seal

The clamping system that is integral to the detectors longevity was tested over the course of two months exposed to atmospheric conditions. When comparing the initial results with those taken 2 months later there was no loss in performance over this period within error. This indicates that there had been no measurable degradation in the detector crystals

over this time. The resolutions for a 661.7KeV peak from the initial testing and those from after two months exposure are shown below in table 10.

Table 10: Comparison of the non-linearity calibrated resolutions of each crystals' initial test and those gathered 2 months after sealing the detector. These resolutions are for a 661.7KeV peak produced by a ^{137}Cs source, the values agree within errors.

Crystal	Initial resolution	Resolution after 2 months
1	7.8±0.1%	7.9±0.4%
2	8.6±0.2%	9.1±0.4%
3	7.4±0.1%	7.5±0.3%
4	7.5±0.1%	7.5±0.3%

5.1.6 Microcontroller Circuit Linearity and Resolution

Microcontrollers like the Arduino Nano BLE33, used in this experiment, have been used in other experiments relating to γ ray detection. A similar experiment conducted in 2018 by C.M Lavelle used an Arduino UNO microcontroller for γ ray spectroscopy [46]. The UNO is a larger microcontroller that is also made by Arduino (double the size of the Nano). The Nano BLE33 has a 4 times faster processor as well as 31 times more flash storage (32KB vs 1MB). Most importantly for this application the ADC resolution of the UNO is 8-bit vs the 12-bit resolution of the Nano BLE 33 [47] [48].

For this reason, the experiment conducted by Lavelle used an external ADC that had 4 channels with a 16-bit resolution and had an operational voltage range of 5V. With this external ADC the UNO based device was able to achieve good instrument resolution of 2±1 ADC channels [46]. This is much better than the 44.5±0.2 ADC channels achieved by the circuit in this experiment. The Lavelle experiment used twisted pairs of wires to

connect the microcontroller to the external DAC, which was done to reduce the noise. This may explain some of the discrepancy between the two devices however as they are different ADCs this cannot be directly compared. With that said it does not appear as though the entire improvement of the Lavelle circuit was due to a superior DAC.

The circuit developed in this project performed very well in terms of linearity. Below 2.9V the maximum percentage nonlinearity was 1.24±0.03%. Above 2.9V however the nonlinearity was a lot worse with the 3V nonlinearity jumping to 2.61±0.04% [46]. This was due to the ADC struggling to accurately compare the input to its reference voltage of 3.3V. As the input tended towards 3.3V the accuracy of this comparison, and the subsequent conversion of the analogue signal to a digital number, would further reduce. In comparison to this project the Lavelle microcontroller circuit achieved a nonlinearity of 4% throughout its operating range.

5.2 Future Outlook

This section will go through the proposed next steps for both the hermetically sealed NaI(Tl) detector and the microcontroller detector circuit. Improvements on the work presented are put forward for further future research.

5.2.1 New Housing Design

As shown in section 5.1.5, the aluminium housing design and clamping system performed well when exposed to normal atmosphere. However, a geometric limitation of the current housing and clamping system is the width it adds to the detector. As shown in Figure 3.4 the current model is designed with a 5mm overhang on all sides, this was experimentally measured as being a 4.4±0.1mm overhang. This is important as the housing is a prototype for a detector that would be used in the HYPATIA array as discussed in section 1. The array requires the detectors to fit together in a close-packed configuration to form rings around the target as shown in Figure 1.2. While the added width does not affect the packing of detectors within individual rings due to each detector in the ring being at a small angle relative to its neighbour. This has an effect however, when packing the rings together this can be seen in the close up of the array shown in Figure 1.2. Any overhang from the main detector body on the sides where two rings meet adds empty space between the rings which has a direct effect on the solid angle coverage and, hence, the gamma-ray efficiency of the array. To reduce this overhang on two sides a new clamping system has been designed. The new design is shown in Figure 5.2.

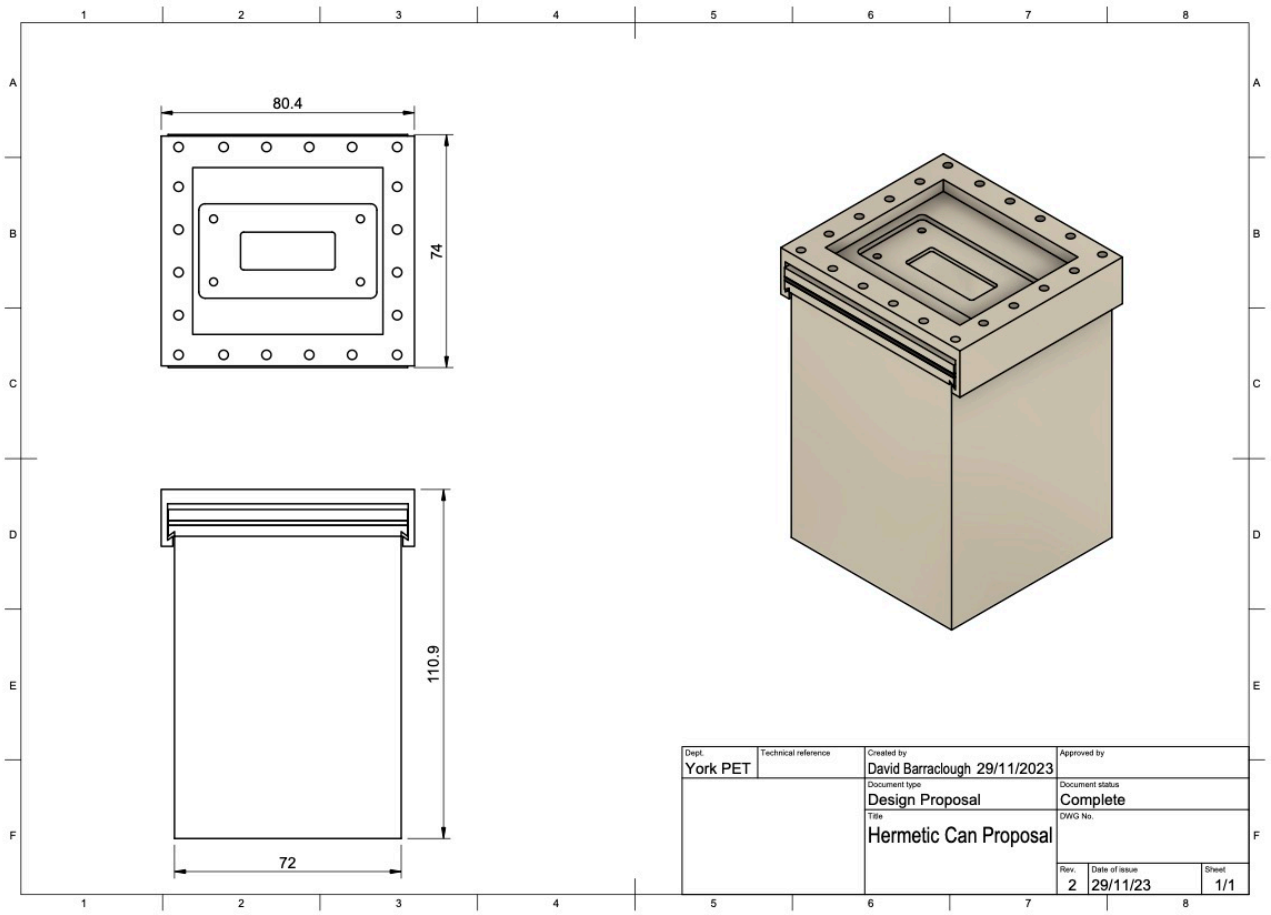

Figure 5.2: Drawing of proposed housing redesign using a single piece sliding clamp. The top view and side view are shown with dimensions labelled.

The new design uses a very similar method of sealing, using a grooved lip to attach a clamp to the lid. This version only has grooves on two sides rather than all four. Instead of having four separate clamps the new design uses a single clamp that slides over the lid. The two sides without the groove now only have a 1mm overhang which is needed to ensure a good seal. Using just two of the version 1 clamps to achieve this same result was discussed but it was concluded that the seal on the unclamped side would be too unreliable. The one-piece clamp removes this issue as it can exert clamping pressure on all four sides using screws as before.

Comparing the two designs in the context of the HYPATIA array, which as Figure 1.2 shows would use six rings of detectors to create its barrel, highlights the advantages of the new design. When considering machining tolerances of 0.1mm the new design would leave 2.0±0.2mm gaps between the detectors opposed to 8.8±0.2mm gaps which the initial design would leave. Below is Figure 5.3, a render of the full array of scintillator detectors intended for HYPATIA, displaying the suggested improvement for the can.

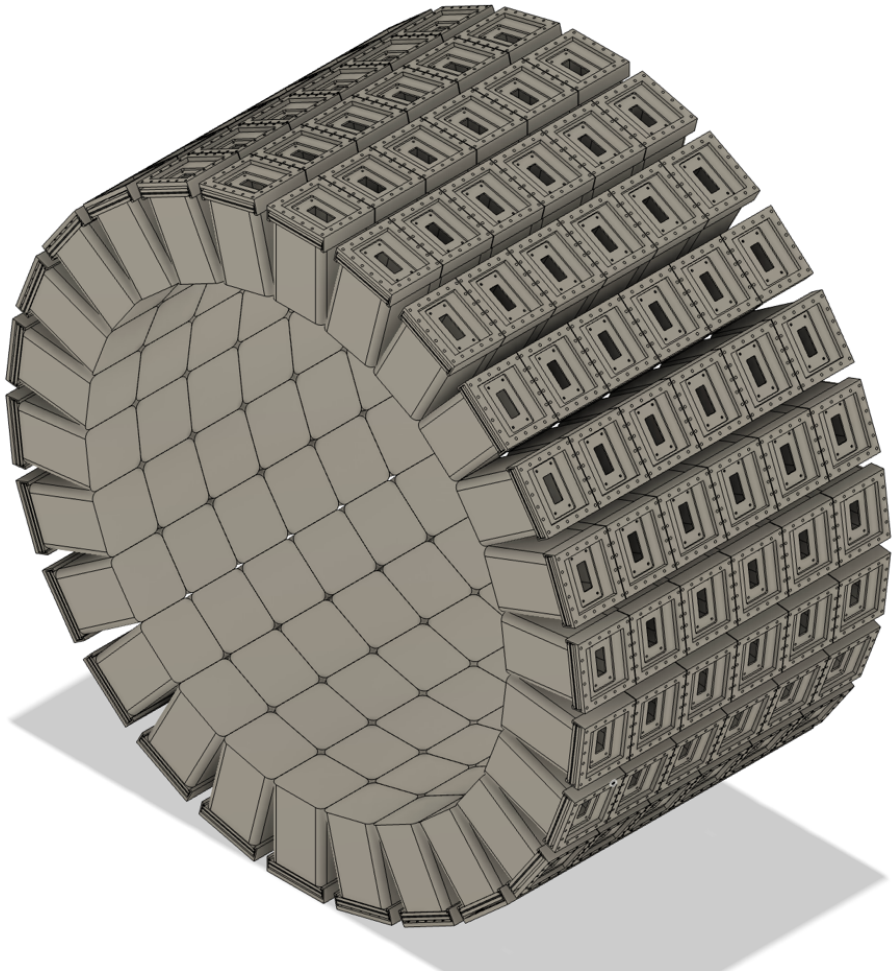

Figure 5.3: Render of the full scintillator detector array for HYPATIA. The array was modelled in Fusion 360 and includes the 0.1mm tolerance expected from the machining of the housing components.

5.2.2. Microcontroller Circuit Next Steps

The prototype microcontroller detector circuit developed in this thesis showed good linearity with a lower than 1% nonlinearity for the majority of its operating range. However, noise and as a result resolution were still an issue. A proposed next step for this circuit was the transition to a PCB design. This would significantly reduce noise that was picked up by the long looping cables on the breadboard prototype.

A design for such a dual channel circuit was produced by the University of York Physics, Engineering and Electronics workshop however, the final product was completed too late for this project to test the circuit. Figure 5.4 shows the PCB. The PCB was designed to slot into an aluminium housing which would further reduce noise and protect the board. A Cremat CR-200 shaping amplifier [49] was also added to each channel, enabling the device to be portable and not reliant on external shaping amps.

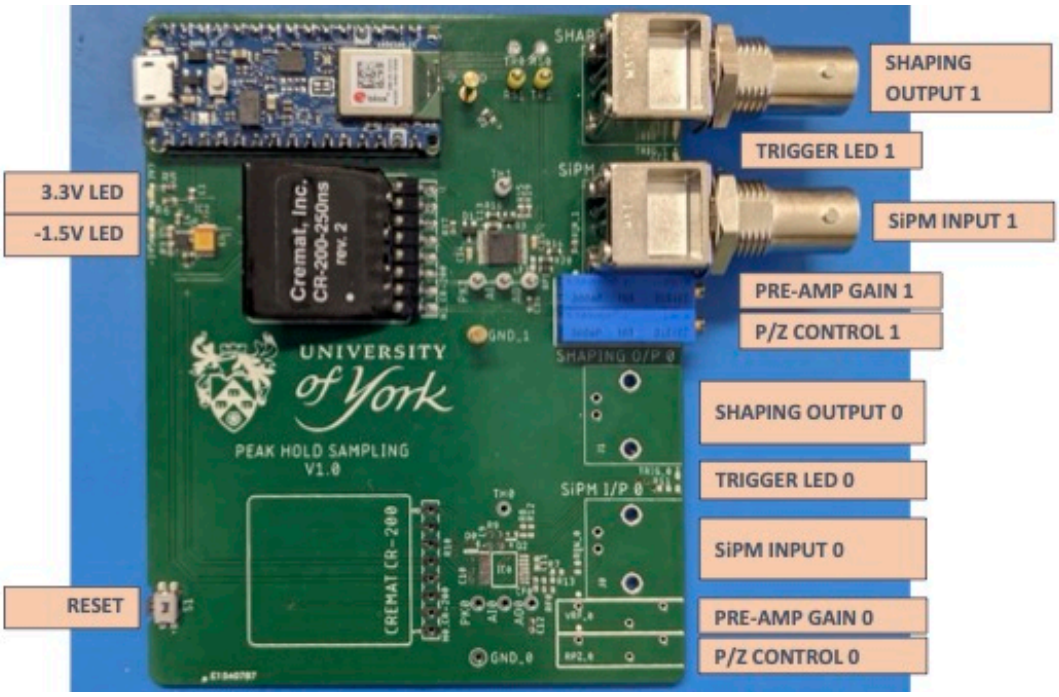

Figure 5.4: Annotated photo of peak hold sampling PCB. Only half of the board has been populated with components. Both channels would run into the same microcontroller. This board was produced by the York PET Electronics Workshop

Data acquisition and exporting was another weakness of the circuit produced in this project. The microcontroller either had to have its performance reduced to stream the data over UBS serial or have short periods of inactivity. While the latter was acceptable for testing the prototype in the lab, this would be a prohibitive disadvantage in the majority of applications. One solution for this problem would be to have a script that would be run on the laptop or computer connected to the microcontroller, that would read the data from the microcontroller's memory. This would allow for direct data streaming without requiring the microcontroller to interrupt or slow its own code loop.

References

[1] E. Rutherford, “The scattering of α and β particles by matter and the structure of the atom,” The London, Edinburgh, and Dublin Philosophical Magazine and Journal of Science, vol. 6, no. 21, pp. 669–688, 1911.

[2] L. Kubetsky, USSR, Author’s Certificate No. 24040, Priority 4, 1930.

[3] V. K. ZWORYKIN, et al, “The Secondary Emission Multiplier – A New Electronic Device”, Proceedings of the Institute of Radio Engineers, vol. 24, no. 3, pp. 351-375, 1936.

[4] L. A. Kubetsky, "Multiple Amplifier," Proceedings of the Institute of Radio Engineers, vol. 25, no. 4, pp. 421-433, 1937.

[5] P. Görlich, “About Composite transparent photocathodes”. *Z. Physik*, vol. 101, pp. 335–342, 1936.

[6] F.C. Nix, “Photoconductivity”, Reviews of Modern Physics, vol 4, no. 4, pp.723-766 1932.

[7] R.S. Ohl, Light-Sensitive Electric Device, US Patent 2402662, Issued 25-06-1946; Filed 27-05-1941.

[8] W. J. Pietenpol, “Junction Rectifier and Photo-Cell” Physics Review, vol 82, no. 1, pp 120-121. 1951.

[9] J. Nishizawa, "PIN Photo-Diode", Japanese Patent# JP1955-8969A, 1952.

[10] A. Goetzberger, et al, “Avalanche effects in silicon p-n junctions. II. Structurally perfect junctions,” Journal of Applied Physics, vol 34, pp. 1591–1600, 1963.

[11] R. Hofstadter, “Alkali Halide Scintillation Counters”, Phys. Rev., vol 74, no.1, pp. 100-101, 1948.

[12] M.J. Weber and R.R Monchamp, “Luminescence of $Bi_4Ge_3O_{12}$—spectral and decay properties”, J. Appl. Phys., vol 44, pp. 5495–5499, 1973.

[13] A. Canning, A. Chaudhry, et al, “First-principles study of luminescence in Ce-doped inorganic scintillators”, Physical Review B, vol. 83, No.12, pp. 125115, 2011

[14] K. Kamada, et al, “Composition engineering in cerium-doped $(Lu,Gd)_3$- $(Ga,Al)_5O_{12}$ single-crystal scintillators”, Crystal Growth Des., vol 11, pp. 4484–4490, 2011.

[15] Takayuki Yanagida, “Inorganic scintillating materials and scintillation detectors”, Proceedings of the Japan Academy, Series B, Physical and biological sciences vol. 94, no. 2, pp. 75-97, 2018.

[16] T Yanagida. Et al, “Comparative study of ceramic and single crystal Ce:GAGG scintillator”, Optical Materials, vol. 35, no.12, pp. 2480-2485, 2013.

[16] S. Takeuchi, et al, “DALI2: A NaI(Tl) detector array for measurements of γ rays from fast nuclei”, Nuclear Instruments and Methods in Physics Research Section A: Accelerators, Spectrometers, Detectors and Associated Equipment, vol 763, pp. 596-603, 2014.

[17] I. Murray, “DALI2+ at RIKEN Nishina Center RIBF”, RIKEN Accelerator Progress Report , vol 51, pp. 158, 2018.

[18] F. G. A. Quarati, et al. "Scintillation and detection characteristics of high-sensitivity CeBr3 gamma-ray spectrometers." Nuclear Instruments and Methods in Physics Research Section A: Accelerators, Spectrometers, Detectors and Associated Equipment, vol 729, pp. 596-604, 2013.

[19] P. Doornenbal, M. Petri et al., Construction Proposal for the HYPATIA project, RIBF NP-PAC-24, 2023

[20] Sun Flower Collaboration [Online], Available: https://www.nishina.riken.jp/collaboration/SUNFLOWER/devices/HYPATIA/index.php

[21] Be, M.M. et al., Table of radionuclides (Vol.3 - A = 3 to 244) 2006

[22] NIST Fundamental Physics Constants [Online] Available: https://physics.nist.gov/cgi-bin/cuu/Value?mec2mev

[23] J.H. Hubbell, S.M. Seltzer, “Cross section data for electron–positron pair production by photons: a status report”, Nuclear Instruments and Methods in Physics Research Section B: Beam Interactions with Materials and Atoms, Vol 213, pp. 1-9, 2004

[24] The Klein–Nishina formula visualisation code, [Online] Available: https://scipython.com/blog/the-kleinnishina-formula/

[25] Interaction of γ -rays with matter, [Online] Available: https://www.fe.infn.it/radioactivity/educational/detection.html

[26] Tibor Jacob Hajagos, et al, High-Z Sensitized Plastic Scintillators: A Review, Advanced Materials, 2018

[27] G. Bizarri, Scintillation mechanisms of inorganic materials: From crystal characteristics to scintillation properties, Journal of Crystal Growth 312, 2010

[28] M. Singh Tyagi, Zener and avalanche breakdown in silicon alloyed p-n junctions I: Analysis of reverse characteristics, Solid-State Electronics, Volume 11, Issue 1, 1968, Pages 99-115, ISSN 0038-1101,

[29] Víctor Moya, Jaime Rosado, “Understanding the Nonlinear Response of SiPMs”, *2024*, arXiv:2401.06581

[30] Andrea L. Lacaita, et al, On the Bremsstrahlung Origin of Hot-Carrier-Induced Photons in Silicon Devices, IEEE Transaction on electrical devices., Vol. 40, No. 3. March 1993

[31] Epic Crystal, NaI(Tl) crystal data sheet, [Online] Available:

[32]

[33] M. Janecek, Reflectivity Spectra for Commonly Used Reflectors, EEE Transactions on Nuclear Science, Vol 59(3), p 490-497, 2012

Spectrometers, Detectors and Associated Equipment, vol. 389, no. 1-2, pp. 81–86, 1997.

[34] Eljen Technology, Silicone Grease EJ-550 Data Sheet, Available Online: https://eljentechnology.com/images/products/data_sheets/EJ-550_EJ-552.pdf

[35] Hamamatsu S14160-6050HS data sheet [Online] Available: https://www.hamamatsu.com/content/dam/hamamatsu-photonics/sites/documents/99_SALES_LIBRARY/ssd/s14160_s14161_series_kapd1064e.pdf

[36] Alexander P. Povilusetal, et al., Vacuum compatibility of 3D-printed materials. J. Vac. Sci. Technol, 1 May 2014

[37] Caen Group, DT5725s Digitiser, Available Online:

[38] Caen Group, DT5485P Desktop Power Supply, Available Online: https://www.caen.it/products/dt5485p/

[39] Caen Group, DT5724 Digitiser, Available Online:

[40] R. Brun and F. Rademakers, “ROOT - An object oriented data analysis framework,” Nuclear Instruments and Methods in Physics Research, Section A: Accelerators,

[41]Arduino Pinout, [Online] Available: https://content.arduino.cc/assets/Pinout-NANOble_latest.pdf

[42] Physics Open Lab, Front-end Electronics for SiPM, Available Online:

https://physicsopenlab.org/2017/11/28/front-end-electronics-for-sipm/

[43]Adafruit MCP4725, 12-Bit Digital-to-Analog Converter, Datasheet, Available Online:

[44] Ortec, Model 572A Spectroscopy Amplifier, Datasheet, Available Online:

[45] Tuchen Huang, et al, NaI(Tl) scintillator read out with SiPM array for gamma spectrometer, Nuclear Instruments and Methods in Physics Research Section A: Accelerators, Spectrometers, Detectors and Associated Equipment, Volume 851, 2017, Pages 118-124

[46] C. M. Lavelle, “Gamma ray spectroscopy with Arduino UNO”, *American journal of physics*, vol. 86, no. 5, pp. 384–394, 2018

[47] Arduino Uno data sheet, [Online] Available: https://docs.arduino.cc/resources/datasheets/A000066-datasheet.pdf

[48] Arduino Nano BLE33 data sheet, [Online] Available: https://docs.arduino.cc/resources/datasheets/ABX00030-datasheet.pdf

[49] Cremat, CR-200 Gaussian shaping amplifier, datasheet, [Online] Available: